DISSERTATION

The role of Nucleoporin Rae1 in cell fate determination

Graduate School of
Natural Science & Technology
Kanazawa University

Division of Natural System

Student ID No: 1824062010
Name: DINI KURNIA IKLIPTIKAWATI
Chief Advisor: Prof. Richard W. Wong
Date of Submission: June, 24th 2021

ACKNOWLEDGEMENTS

In the name of Allah, the Most Gracious and the Most Merciful. All praises to Allah and His blessing for all the opportunities, trials and strength that have been showered on me to complete this thesis writing. My humblest gratitude to the holy Prophet Muhammad (Peace be upon him) whose way of life has been a continuous guidance for me.

First and foremost, I would like to genuinely grateful to my supervisor Prof. Richard W. Wong for his persistent encouragement and warm spirit toward the completion of this thesis. It has been a great pleasure and honour to have him as supervisor who always guide, understand, motivate, and support me patiently during my Ph.D program. I could never have done it without his significant help.

I would also like to give appreciation to Dr. Masaharu Hazawa, Dr. Akiko Kobayashi, Dr. Lim Kee Siang, Dr. Firli Primula Dewi, Dr. Mahmoud Shaaban Mohamed Abdelrasoul, and Dr. Hartono for their valuable training and advice to enrich my theoretical and technical abilities.

I also had the pleasure of working with our team mates: Yoshihiro Iga, Kie Sakai, Katsushi Morikawa, Hanbo Wang, Yuki Iwashima, Hiroya Kondo, Goro Nishide, Koki Kato, Elma Sakinatus Sadjidah, Qiu Yujia, Kei Makiyama and Ratna Nurarifa who have been so kind and helpful in giving me support during my daily laboratory life.

I am also grateful to the generous financial support from the Ministry of Education, Culture, Sports, Science and Technology (MEXT) for making my dream comes true through oversea study in Japan. Also, it would be inappropriate if I omit to mention the gratitude to all my Indonesian friends in Kanazawa, especially the MEXT awardee.

My acknowledgement would be incomplete without thanking the biggest source of my strength; my family. The blessings of my father H. dr. Moelyadhi, Sp.THT and my mother Hj. Dra. Tri Yuliani, M.M. and the love and care of my sister Vita Shany Nugrahaeni, S.T. and her husband, Dr. Eng. Favian Dewanta, S.T., M. Eng, whose love and their support are with me in whatever I pursue. As

to my sweet son Muhammad Rafid Ghiffari Rendradinata, my love and longing for him are beyond words. Finally but definitely not the least, I owe my deepest gratitude to my dear husband drh. Dedy Rendrawan, M.P. I am forever thankful for his unconditional love and his sacrifice to bear the pressure both from working and living during my study, while always available to embrace all of my ups and downs. I dedicate this book for him.

LIST OF CONTENT

LIST OF TABLE AND FIGURES

ABBREVIATIONS

DAPI	4′,6-diamidino-2-phenylindole
DMEM	Dulbecco's Modified Eagle's Medium
FG	phenylalanine-glycine
HPG	hyperbranched polyglycerol
hrRNPA1	heterogeneous nuclear ribonucleoprotein A1
INM	inner nuclear membrane
IP	immunoprecipitation
MS	Mass Spectrometry
ND	Nanodiamond
NE	nuclear envelope
NEBD	Nuclear envelope breakdown
NuMA	nuclear mitotic apparatus protein
NPC	nuclear pore complex
Nup(s)	nucleoporin(s)
ODT	Optical Diffraction Tomography
ONM	outer nuclear membrane
PBS	phosphate-buffered saline
PCR	polymerase chain reaction
qPCR	quantitative real time PCR
Rae1	mitotic checkpoint regulator
RI	refractive index
RT-PCR	reverse transcription-PCR
siRNA	small interfering RNA
SDS-PAGE	sodium dodecyl sulfate–polyacrylamide gel electrophoresis
SMC1	structural maintenance of chromosomes subunit 1
SARS-CoV-2	Severe acute coronavirus respiratory syndrome coronavirus-2
VSV	Vesicular stomatitis virus
ZEB1	Zinc Finger E-Box Binding Homeobox 1

CHAPTER I.

Rae1 in Cancer: The preliminary study of the role of Rae1 in breast cancer

I.1. ABSTRACT

Nuclear pore complexes (NPCs), alongside as having the main function as nucleocytoplasmic trafficking, have also implicated in numerous basic cellular processes including mitosis, differentiation, chromatin organization, epigenetic regulation and so forth, which correlated with many diseases. Previously, we and others showed that nucleoporin Rae1 is a binding platform for NuMA, cohesin subunits SMC1 to prevent aneuploidy during mitosis. Bioinformatic data analysis from The Cancer Genome Atlas (TCGA) showing that Rae1 is extensively amplified and overexpressed in several solid cancers including colon and breast cancer respectively. Here, we first performed transcriptomic and proteomic study of Rae1 in MCF7 breast cancer cells to provide in depth-understanding about the global change of differentially expressed genes. We performed RNA sequence from Rae1 depleted cell, and mass spectrometry (MS) of Rae1 immunoprecipitates from MCF7 cell lysates. From the Phenotypic assay, our work suggested that Rae1 might be important to overcome susceptibility of apoptosis in MCF7 as depletion of Rae1 lead to the increasement of apoptotic marker under the anoikis condition.

Keywords: Rae1, MCF7, mass spectrometry, apoptosis

I.2. INTRODUCTION

I.2.1. Breast cancer in human

Malignant tumours (cancers) occupy the main mortality rate and an obstacle to raise the probability of life in many countries worldwide. The number of breast cancer cases has reported exceeds the lung cancer as per the "GLOBOCAN 2020" with an estimated 2.3 million new cases and considerably high death rates in developing countries compare to developed countries (15.0 vs 12.8 per 100.000) [1].

Studying breast cancer in human is often closely related to the concept of the basis of molecular and cellular biology. This disease has heterogenicity that can be classified into several subtypes. Appropriate classificacion of breast tumour is crucial to understand the etiology, clinical course prediction, and therapeutic strategy. The distinction into relevant subtypes in breast cancer can be established based on several parameters of the patients on the basis of phenotypic or genotypic traits of the neoplasm itself, such as staging, grading, as well as histological and genetical profiling [2].

Staging and grading of tumour can be described differently, despite their correlation in giving, guiding and predicting the disease course as well as treatment strategy. The stage of breast tumour refers to its extent and spreading, commonly defined by the volume of the tumour including the involvement of the lymph node and other affected organs. In other hand, tumour grade gives a definition of how close or far the morphological feature of the breast tumour compare to normal breast tissue, microscopically. Staging of the tumour (I-IV) entails some tumour cell penetration outside of the basal membrane, thereby referred to as tumours invasiveness. Tumour with as highest as no more than 2 cm in diameter belongs to the stage I, while the one showing more aloof mestastasis is considered as stage IV. The grade of tumour is measured semi-quantitatively according to (1) duct formation score, (2) proliferation events, and (3) variability of nuclei; hereinafter determined as grade 1-3 based on the combination of these

three characteristic. Grade 1 denotes a tumor made up from breast cells that differentiate finely with an appearance as normal and do not develop quickly, grade 2 denotes a tumor made up from breast cells that differentiate moderately, whereas grade 3 denotes a tumor made up from breast cells that differentiate poorly followed by the aggressive spreading [3].

Breast cancer can be also characterized according to histological feature including cells organization and growth pattern. The most common type based on this category are ductal and lobular carcinoma where (with respect to 'on site' lesion) ductal carcinoma and lobular carcinoma in situ (DCIS and LCIS) account for 80-85% and 5%, respectively. Additionally, regarding to disease invasiveness, invasive ductal and lobular carcinoma (IDC and ILC) are as much as 70-73% and 13-16%, respectively. About 15% of the rest are made up of a group with heterogenicity, each of which constitutes for approximately no more than 2% invasiveness and has yet to be precisely classified. Likewise, it can be postulated that it is common for the tumours to make advance stage and/ or grade progression over time if left untreated as illustrated in **Figure 1** [3].

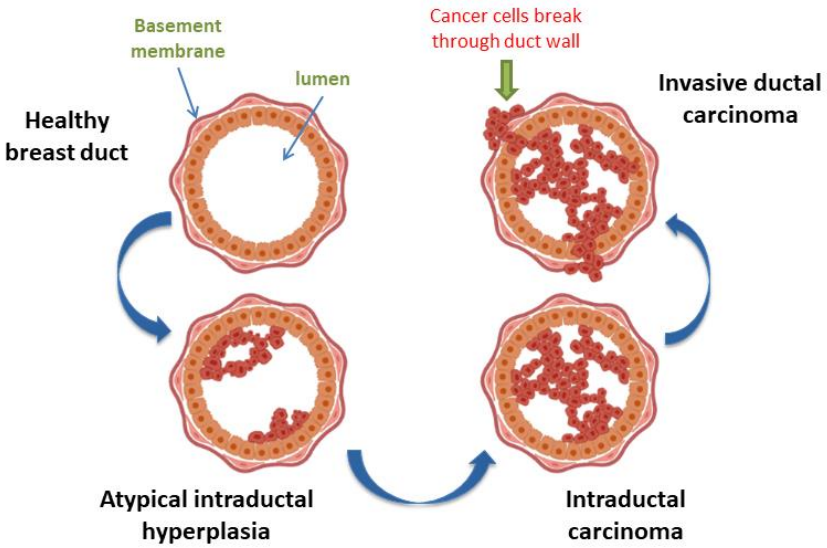

Figure 1. Progression of breast cancer (made with biorender)

Other discrimination of breast cancer subtype are related to the expression of the key receptors that has been classically shown including estrogen receptor (ER), progesterone receptor (PR), and Human epithelial receptor 2 (HER2) (**Table 1**) [3,4]. The importance of ER expression has been mentioned in some studies [5-11]. Tumour markers that can be used for individual assay such as ER (most importantly), epidermal growth factor receptor (EGFR), p53, PR, and HER2 give benefits for helping decision regarding to the treatment strategy and clinical prognosis. Tumours with high ER concentration or those positive for both ER and PR have the highest chance of positive clinical impact from hormonal medications [3].

Table 1. Breast cancer cell line subtyping on the basis of hormone receptor expression marker

No	Hormone receptor status	Cell lines
1	ER+	IBEP2, LY2, MDA-MB-134, MDA-MB-175, MDA-MB-175VII, ZR75B, KPL1, MDA-MB-134VI
2	HER+	HCC202, HH315, HCC2218, HH375, KPL-4, HCC1008, SKBR5, HCC1954, HCC1569, SUM-225CWN, SUM190PT, UACC893, OCUB-F, MDA-MB-453, SKBR3, AU565
3	ER+, PR+/-	BT4-83, CAMA1, HCC712, MDA-MB-415, ZR751
4	ER+, PR+	EFM19, HCC1428, **MCF7**, T47D
5	ER+, PR+/-, HER2+	MDA-MB-361, UACC812
6	ER+, PR+, HER2+	BSMZ, BT474, EFM192A
7	PR+/-, HER2+	21MT1, 21MT2, 21NT, 21PT
8	PR+, HER2+	IBEP1, IBEP3
9	ER-, PR-, HER2-	BT20, CAL148, DU4475, EMG3, HCC1143,

	Triple negative A	HCC3153, HCC2157, HCC70, HMT3522, HCC1187, HCC1806, HCC1937, HCC1599, MDA-MB-468, SUM229PE , MFM223, SUM185PE, KPL-3C, MA11, MDA-MB-435, MDA-MB-436,
10	ER-, PR-, HER2- Triple negative B	BT549, CAL120, CAL51, CAL851, HCC1395, HCC1739, HCC38, HDQ-P1, Hs578T, MDA-MB-157, MDA-MB-231 SKBR7, SUM102PT, SUM1315M02, SUM149PT, SUM159PT

Breast cancer with ER+ is associated with genes and proteins involved in proliferation and cell cycle regulation. Higher expression of cyclin-dependent kinase inhibitors p21 and p27, cyclin D1, and apoptosis inhibitor bcl-2 are brought by this subtype. Meanwhile ER- brings higher expression of p53, cyclin E, and proliferation indicator [12-17].

Between the basal and luminal of the cell lines, there is a heterogenous cells fill in the space of this attribute, which is so called as tumour cell with HER2+. As highlited by ER- and HER2+; this HER2+, on chromosomal region 17q12 encompassing genes including HER2, STARD3, C17Orf37, PERLD1, and GRB7, share the same over-represented genomic profile. Overexpression of HER2+ tumours are more likely to show a more advanced stage and grade, hence are correlated with significant worse survival, however they still may have benefit to chemotherapy with anthracycline-based neoadjuvant [2,4].

Breast cancer cell lines with ER-, PR- and HER2- (triple negative) are differentiated as basal A (luminal-like) and basal B (basal-like). The basal keratins expression gene such as KRT4/5/6/13/14/15/16/17 that represent the basal tumours' core are best described the triple negative A. Meanwhile the CD44+CD24- ; together with VIM (a migration marker) are represented the triple negative B. These markers can also be employed for metaplastic and/or claudin-low model of breast cancers [4].

I.2.2. Structure and function of Nuclear Pore Complex

Discovered in the 1950s, Nulear Pore Complexes (NPCs) were the most enormous complexes of protein in eukaryotic cells, approximately around 60 and 90–120 MDa in in yeast and humans, respectively. It has minimum 456 individual protein molecules and are consisted of ~30 types of nucleoporins (Nups). NPCs have an eightfold rotational symmetry, as well as a membrane-embedded scaffold structured around a central transport channel, cytoplasmic rings, nuclear rings, and eight filaments linked to each ring (**Figure 2**). The nuclear filaments are linked to a nuclear ring in a distal part to form the NPC's "nuclear basket." [18,19].

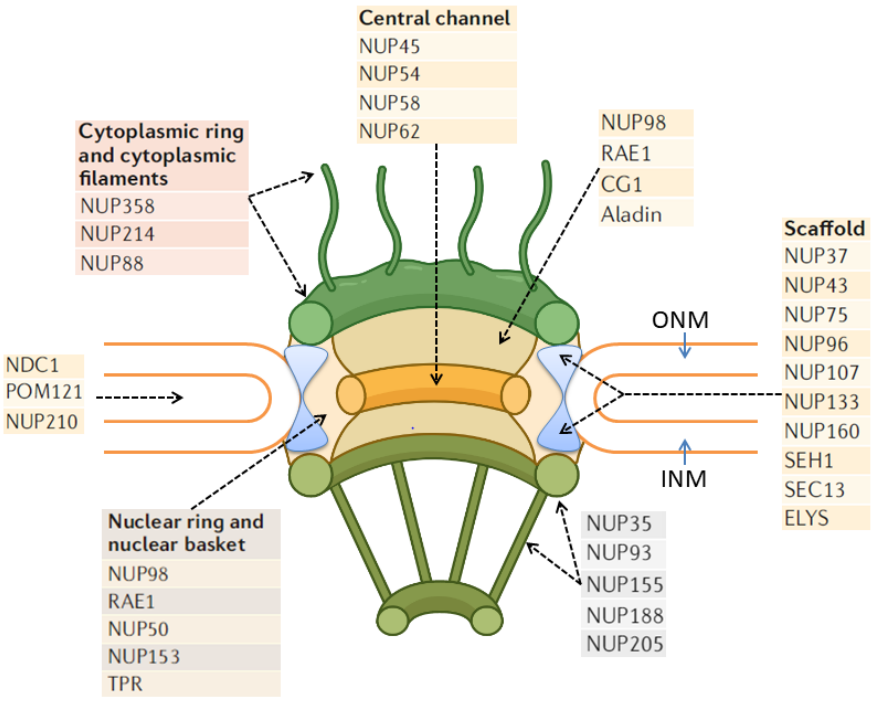

Figure 2. Illustration of schematic NPCs structural organization (made with biorender)

A set of domains of NUPs are consisted of transmembrane (found in only yeast and four mammalian), α-helices, β-propellers, phenylalanine and glycine (FG) repeats and beta-transducin repeats (WD) domains with FG repeats are the most common domains. NUPs carrying 4 to 48 FG repeats fill the central channel

of the NPC, thereby forming a meshwork that is responsible to control nucleocytoplasmic transport and that determines the pore permeability limit. NPCs act as the gateways that responsible to connect and control the transport of molecule between cytoplasm and nucleus. Ions and small molecules passively move in a diffusion manner to pass the pore, however larger molecules (more than 40–60 kDa) need to be actively generated by transporters [20,21].

The most crucial type of transporters is known as the karyopherin family where its members are in charge in controlling the NE and NPC assembly and also the replication activity. These proteins with around 100 kDa are commonly differentiated into importins and exportins group. The importins manage import of molecules from the cytoplasm to the nucleus, whereas the exiting of this molecules from the nucleus are supported by the exportins. Members of the karyopherin family have three major characteristics which have a significant impact on controling the cargo transportation. They are: (1) binding to cargos to carry them, (2) interacting with FG repeats (which run along the NPC's inner part) if they are to pass through the NPC, and (3) asking a source of energy for ongoing transport, obtained through associations with RAN GTPase-bound-GTP (RAN-GTP). Karyopherins are competent to attach to cargos which facilitates their passage through the channel.

To regulate the in-and-out moving of the cargos, karyopherins also need to initiate post-translational modification. To do so, importins bind to nuclear localization sequences/NLSs (some specific sequences of the cargo) while the exportins bind to nuclear export sequences (NESs). NLSs are separated into 1). classic NLSs (cNLSs) group where the lysine and arginine are loaded into its amino acid, and 2). Non classic NLSs (nNLS) where they are deficient in basic amino acid residues and acted inveresely to cNLS. Two forms of cNLSs including monopartites and bipartites are exsisted. One of them brings a single basic amino acid strech and the other one brings several of those stretches, respectively. Exported cargos that are decorated with NESs usually having Leu-rich or the hydrophobic amino acids [21].

The transport receptor binds with the tiny RAN-GTP inside the nucleus to deliver the cargo after nuclear import. Likewise, RAN-GTP is required for the formation of the receptor–cargo complex in nuclear export, which is dependent on GTP hydrolysis for cargo delivery. Export complexes are disassembled at the cytoplasmic filaments of the NPC by the activities of RAN-binding protein 1 (RANBP1) or RANBP2 and RAN GTPase-activating protein (RANGAP). Together they induce RAN to hydrolyse bound GTP, allowing export complex dissociation irreversible. As a result, nucleocytoplasmic transport directionality is achieved via a RAN-GTP gradient between the nucleus and the cytoplasm [20,21]. NPCs can also influence gene expression indirectly by controlling RNA and gene regulatory factor trafficking via the nuclear envelope. NPCs and NUPs also have a direct function in transcriptional regulation [21]. Although the underlying molecular processes are not fully known, NPCs appear to regulate gene expression in a various ways.

I.2.3. Insight into nucleoporin Rae1

Rae1 is a conserved protein previously identified as an mRNA export protein of 41 kDa which was cross-linked to poly(A)-containing mRNA, therefore known also as Mrnp41. The Mrnp 41 protein is the likely homolog of Rae1 of *Schizosaccharomyces pombe* and Gle2p of *Saccharomyces cerevisiae* (hence, designated also as Gle2). It is also a homologue of spindle checkpoint protein of BUB3 [22,23]. It contains four tryptophan-aspartic acid (WD) motifs, as well as having the localization inside the nucleoplasm, in the membrane of nucleus, and forming the structure like a meshwork in cytoplasm. Rae1 has been shown to be presented in both nucleus (particulary enveloped) and cytoplasma by immunoblotting and cell fractionation. This gene is considered to be associated in the exchange between nucleus and cytoplasm, and in directly or indirectly attaching cytoplasmic mRNPs to the cytoskeleton. Moreover, an alternative splicing variants of transcription which encodes the similar protein for this gene can also be found [24].

Rae1 binding to the GLEBS motif of Nup98 allows them to connect and collaborate in mRNA export or spindle assembly to prevent chromosomal mis-segregation [25-30]. Rae1 depletion and overexpression equally promote the development of multipolar spindles, which may be rescued by NUMA depletion or co-overexpression, respectively. Imbalances in the interconnections of NUMA, SMC1, and Rae1 result in the development of multipolar spindles and aneuploidy, increasing genomic instability and driving tumorigenesis. [25,26].

The Nup98 GLEBS motif folds into an N-terminal 10-residue coil region, which is followed by β1 and β2 strand, which are joined to the C-terminal -helix A by a 13-residue linker segment. The Nup98 GLEBS hairpin attaches to the top face of the Rae1-propeller domain and covers the whole surface. The GLEBS pattern is most commonly found on the Rae1- β-propeller [30].

Rae1 and Nup98 are spatially compartmentalized in both the nucleus and cytoplasm fractions. The combination mediates BMAL1 shuttling and regulates the consistent speed of the circadian clock between the nucleus and cytoplasm [32]. Furthermore, Rae1 was discovered to mediate ZEB1 expression in breast cancer through facilitating epithelial-mesenchymal transition. [33].

I.2.4. Identification of potential genes candidate is in Rae1-breast cancer regulation

To date, several studies have been conducted to determine the mechanisms that are important for breast cancer development. Data analysis from transcriptomic and proteomics studies are widely used to support the knowledge of cellular processes, progression of the disease, and the relationship between gentic and phenotipic maaterial. Several pathways that extensively studied related to Rae1 in cancer including cell cycle, mitotic, RNA metabolism, gene expresion and transcription, disorders of transmembrane transporters and more, have been purposed. As finding the bonafide theraphy in breast cancer continued to encounter adversity, attention to the emerging field of study called epigenetics are growing more nowadays. This would have aroused attention in the development

of antitumor medicines called epitherapeutics that significantly change the cancer cell's aberrant chromatin structure and gene-expression patterns.

The underlying cause of cancer is utterly complex that might include both genetic and acquired factors. Several studies suggested that interactions of Nups with diverse histone modifying enzyme was possible to occured by affecting chromatin condensation directly, or giving signal to engage proteins that mantain chromatin compaction including transcriptional processes afterwards [49]. In general, epigenetic processes include 1.) DNA methylation, 2.) histone modification, and 3.) noncoding RNA. The components involved in various alteration patterns are classified into three roles: 1.) writers, 2.) readers, and 3.) erasers. Enzymes that correlated with an additional or removal of chemical groups from DNA or histones are referred to as “writers” and “erasers,” respectively. The “readers” can identify the changed of DNA or histones. The epigenome works with other regulatory factors, such as transcription factors and noncoding RNAs, to govern the expression or repression of the genome in order to facilitate numerous bioactivities. Cellular signaling networks and external stimuli can also influence epigenetics. Such consequences are both transient and long-lasting. Considering the significance of epigenetics in regulating cell activities, it is critical to get a better knowledge that underlie the aberrant epigenetic processes. [34].

Study of histone acetylation has lead to the concepts that the first histone acetyltransferases (HATs) and histone deacetylases (HDACs) are not only for gene regulation, therefore many researchers urged to test various transcription factors. HDACs have been identified as being increased in various tumours and abnormally appointed to DNA upon chromosomal translocations, notably in blood cancers [35,36]. firstly found as inducers of modified cell growth arrest and cell death, inhibitors of Zn2+-dependent HDACs were then recognized as inhibitors of HDAC expression. However, despite being inadequately studied, the selectivity of HDAC inhibitors toward tumor cells has contributed to their establishment as chemotherapeutic medicines [37].

I.3. MATERIALS AND METHODS

I.3.1. Cell culture

To propagate human MCF7 cell line, the medium was prepared as DMEM + 10% (v:v) fetal bovine serum (Life Technologies, 10082147) + 50 U/mL penicillin-streptomycin (Nacalai Tesque, 26253-84). The medium for human normal breast MCF10A cell line was basic MCF7's medium but with additional supplementation including horse serum (Invitrogen# 16050-122) in 5% final, EGF (Peprotech) in 20mg/ml final, hydrocortisone (sigma#H-0888) in 0,5mg/ml final, Cholera toxin (Sigma#C-8052) in 100ng/ml final, and insulin (Sigma#I-1882) in 10µg/ml final. Cells were maintained at 37°C with 5% CO2 inside the incubator.

I.3.2. RNA interference by small interfering RNA (siRNA)

siRNA for Rae1 was constructed (Invitrogen) to target nucleotides 343-367 of human Rae1 mRNA (GenBank Accession No. AK292247) and siRNA for control was purchased from Santa Cruz Biotechnology (sc-37007). Transfection of siRNA was carried out by transfection reagent Lipofectamine 2000 (Invitrogen, 11668019). MCF7 cells were seeded in 6-well plates at a density of 1×10^5 cells per well. Transfected cells were incubated for 72 hours and then collected for experiments.

I.3.3. Antibodies

Anti-Rae1 (mrnp41) (Santa Cruz Biotechnology, sc-374261), anti-PARP1 (Santa Cruz Biotechnology, sc-7150), anti-ACTB (Santa Cruz Biotechnology, sc-47778), rhodamine red goat anti-mouse (Invitrogen, R6393), anti IgG mouse-Isotype control (Cell signaling technology, 5415S) were used.

I.3.4. Immunostaining and super-resolution imaging

The 6-well plates equipped by glass coverslips were prepared to culture MCF7 and MCF10A cells. Cells on coverslips were then washed with PBS (137 mM NaCl (Nacalai Tesque, 31320-34), 2.7 mM KCl (Sigma, P9541), 10 mM Na2HPO4 (Wako, 198-05955F), 1.8 mM KH2PO4 (Nacalai Tesque, 28736-75) and fixed for 30 minutes with 4% paraformaldehyde in PBS. The washing step with PBS was repeated, and cells were permeabilized with 0.3% Triton X-100 (Nacalai Tesque, 35501-15) in PBS for 3 minutes. Cells were washed again before blocked in PBS with 4% BSA (Wako, 015-23295) at room temperature for 30 minutes. Incubation overnight of the coverslips were performed in 4% BSA/PBS supplemented with primary antibodies at dilution of 1:500. Next, cells were rinsed and the incubation with secondary antibodies were performed in 4% BSA/PBS at dilution of 1:500 dilution at room temperature for 2 hours. After PBS washing, The surface of coverslips with cells was then attached on slides and mounted by ProLong Diamond Antifade reagent with DAPI (DAPI; Invitrogen, P36941). The observation was performed using confocal laser-scanning microscope with 60X PlanApo/1.45NA DIC objective, as previous protocol [42]. The manufacturers of each materials for immunofluorescnence are as described in the reference paper.

I.3.5. Protein extraction and western blotting

To extract the protein, 100 µl lysis buffer (20 mM HEPES (Sigma, H3375-250G) [pH 7.4], 350 mM sodium chloride, 1.5 mM magnesium chloride, 1 mM ethylene glycol-bis (β-aminoethyl ether)-N,N,N',N'-tetraacetic acid (EDTA; Nacalai Tesque, 15214-92), 10% [v/v] glycerol, 1% Triton X-100, 0.2 mM sodium orthovanadate (Sigma-Aldrich, S6508), and 1 mM phenylmethylsulfonylfluoride (PMSF; Fluka, 78830), supplemented with proteases and phosphatases inhibitors cocktails (Roche, 11697498001)) was used to disrupt 6 x 10^5 cells. The lysates were centrifuged at 14.000 X g at 4 ^oC for 10

minutes to obtain supernatants which were then separated using SDS PAGE and followed by gel transfer using PVDF membranes. The membranes were then incubated overnight by primary antibody and secondary HRP-conjugated antibodies (Millipore, 12–348, and 12–349), subsequently. Using the suitable HRP substrate (Millipore, WBKLS0500), the proteins were detected via chemiluminescence. To capture the images, a LAS-4000 image analyzer was utilized.

I.3.6. Immunoprecipitation (IP) coupled by Mass spectrometry

Following the collection of cells post 72 hours of transfection, cells were lysed by RIPA buffer (50 mM Tris-HCl, 150 mM NaCl, 1% Triton X-100, and 0.1% sodium dodecyl sulfate) supplemented with EDTA-free protease inhibitor cocktail (Nacalai tesque, 04080). Sonication was performed onto the lysate at 15 seconds x 2, followed by centrifugation at 16.000 x g at 4°C for 10 minutes. The antibodies (5 μg) and Dynabeads protein A/G were added to the supernatants. The samples were then rotated at 4 ^{o}C for overnight incubation time. On the subsequent day, the beads were washed using lysis buffer and repeat for 3 times. Immunoblotting was then used to examine whole-cell lysates.

I.3.7. Anoikis assay

After 48 hours of transfection, cells were seeded in the Costar ultra-low attachment 6-well plates (Corning). Floating cells after 24 and 48 hours incubation in the medium were then collected to tube, and centrifuged to obtain the pellets. Cell pellets were resuspended in lysis buffer to further analyzed by western blotting for apoptotic marker detection.

I.4. RESULTS

I.4.1. Rae1 is overexpressed in breast cancer

In our preliminary study, the analysis of mRNA expression level was carried out from cbioportal (http://www.cbioportal.org). Using data from METABRIC & TCGA, we found that amplification and gain was the first and second common abnormalities (**Figure 3**), suggesting breast cancers prone to show over-expression of Rae1

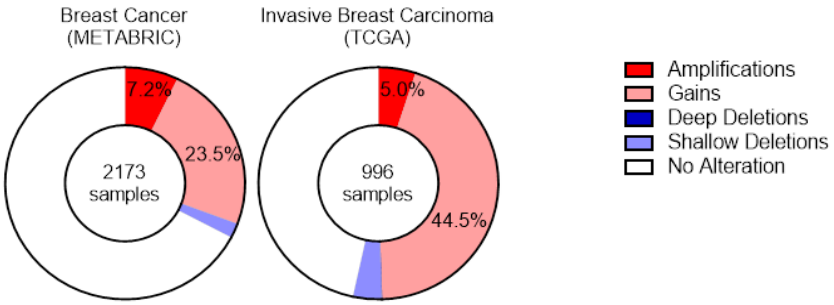

Figure 3. Rae1 abnormality in breast cancer.

Further, we compared the protein levels of Rae1 between breast cancer cell line MCF7 and normal breast cell line MCF10A by western blotting analysis (**Figure 4**). Consistent with in-silico data, the expression levels of Rae1 in MCF7 was elavated in MCF7 comparing to that in MCF10A.

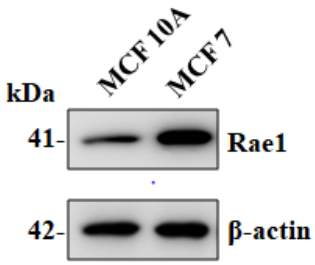

Figure 4. Endogenous Rae1 protein of MCF10A and MCF7 by western blotting

I.4.2. Rae1 prevents anoikis in MCF7 cells

We next asked whether over-expressed Rae1 is functionally involved in resistance to anoikis, which plays a pivotal role during progression of cancers [48]. After introducing siRNA, MCF7 cells were seeded on the anchorage resistant plate for 96 and 120 hours, and detected cleaved PARP, a hallmark of apoptosis, by WB (**Figure 5**). Rae1-depleted MCF7 cells showed marked increasement of cleaved PARP1, suggesting the role of Rae1 in preventing anoikis.

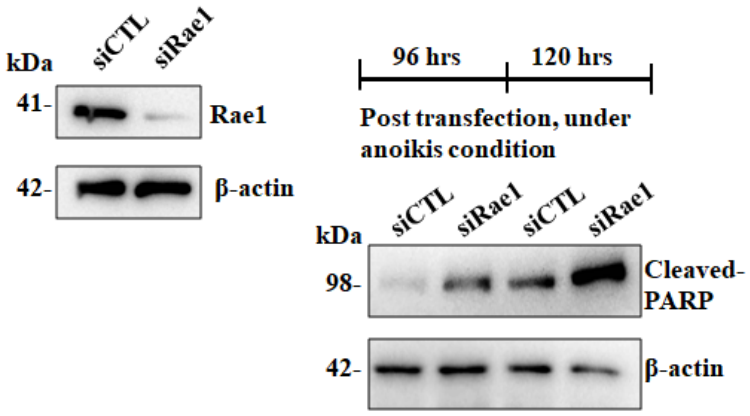

Figure 5. Cleaved PARP protein level by western blotting under anoikis conditions following Rae1 knockdown in MCF7.

I.4.3. The biological processes and signaling pathways regulated by Rae1 in MCF7 cells.

In order to understand the biological processes and signaling pathways upon Rae1 knock-down in MCF7 cells, RNA-seq analysis was performed in MCF7 cells silenced for Rae1 (**Figure 6**). Gene ontology (GO) analysis revealed that loss of Rae1 increased a subset of genes highly enriched in processes regulating type I interferon related events, positive regulation of actin filament bundle assembly and cell death, and gland development (**Figure 6.A**). Pathway enrichment analysis indicated beta-catenin, recombination and methylation, rRNA

expression, SRC familiy kinase pathways were affected by Rae1 knock-down (**Figure 6.B).**

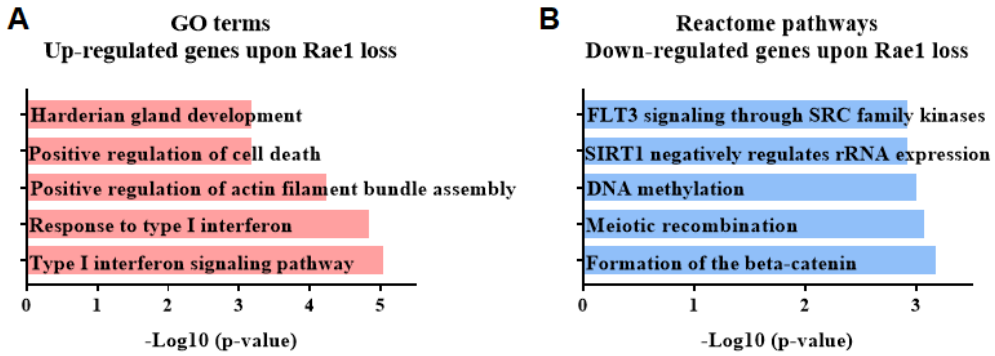

Figure 6. A. GO analysis of the upregulated genes upon Rae1 depletion. **B.** Pathway analysis of the downregulated genes after Rae1 knockdown.

I.4.4. Over-expressed Rae1 localized in nucleplasm in MCF7 cells.

The importance of Rae1 in cancer cell biology has been highlighted [41], however, subcellular dynamics of Rae1 in breast cancers remain unexplored well. In order to determine subcellular localization of Rae1 in breast cancer cells, we next perfomed immunofluorecent confocal microscopic analysis of Rae1 using both MCF7 and MCF10A cells **(Figure 7**).

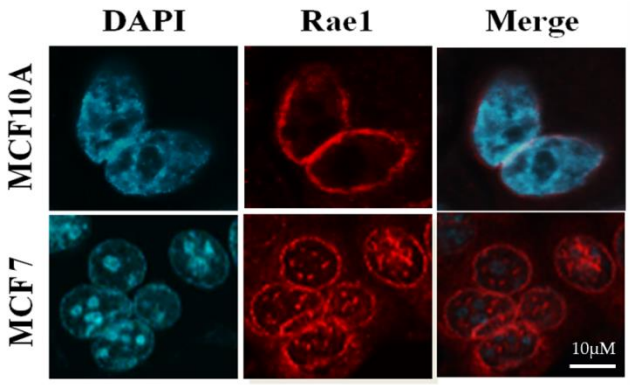

Figure 7. Rae1 localization in MCF10A and MCF7 by Immunofluorescence.

Notably, Rae1 in MCF7 cells localized in both nuclear membrane and nucleoplasm while the localization of Rae1 was mainly in the nuclear membrane in MCF10A, suggesting the cancer specific of Rae1 inside nucloplasm.

I.4.5. Identification of Rae1 binding partners from Mass Spectrometry

Since Rae1 is localized in nucleoplasm, we hypothesized that Rae1 might be involved in transcriptional or epigenetic function, and are inspired to see Rae1 binding partners in breast cancer cells. Therefore, we utilized mass spectrometer (MS) to obtain peptide mass profiles from silver-stained protein in MCF7 (**Figure 8**), where several protein interactors of Rae1 were selected based on the peptides that give high peptide spectrum match (PSM) score [39].

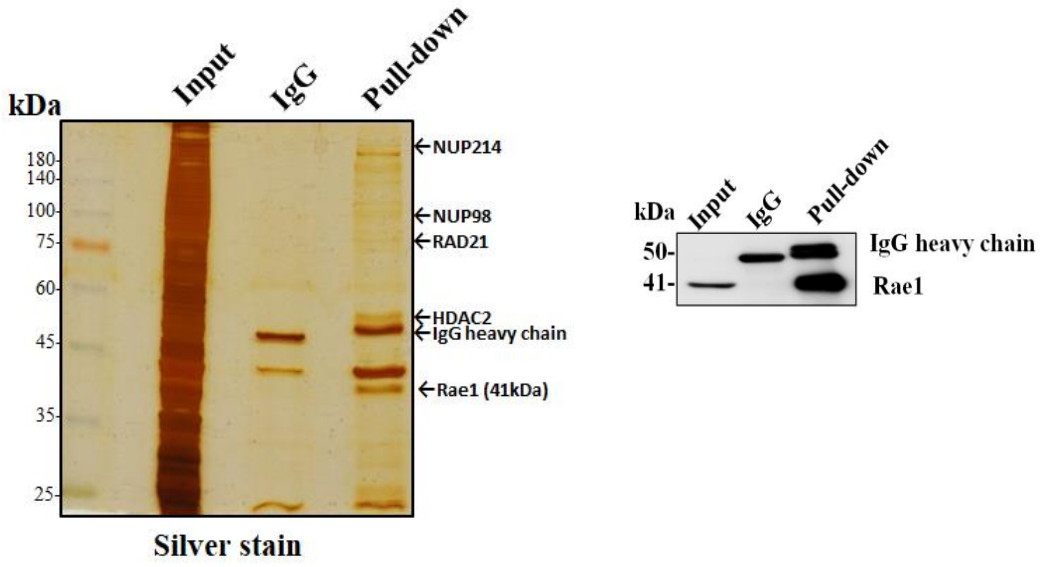

Figure 8. Silver staining and identified binding proteins predicted from from mass spectrometry analysis.

Figure 9 shows the candidates for the query peptides. Unsurprisingly, we identified several established binding protein partner of Rae1 including Nup98 [38]. Importantly, we identified several epigenetic regulator such as HDAC2 and Rad21. These results imply that Rae1 might be involved in epigenetic regulation by collaborating newly identifed epigenetic regulators.

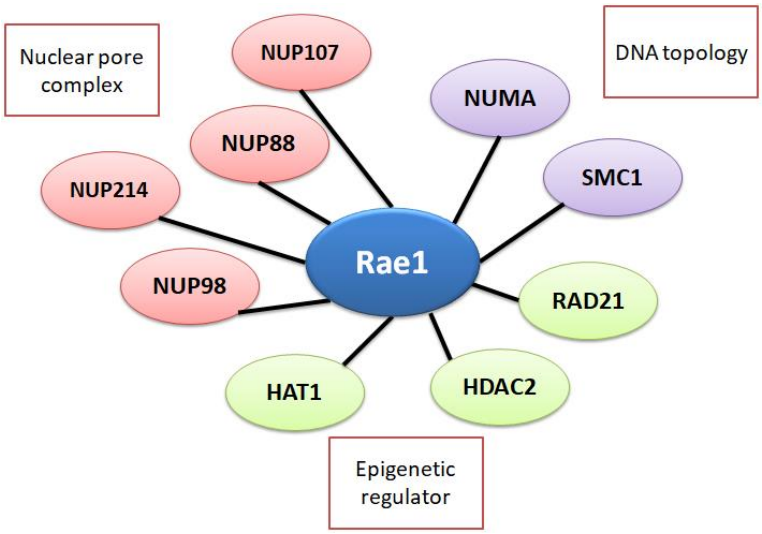

Figure 9. Protein partners of Rae1 selected from Mass Spectrometry

I.5. DISCUSSION

Here, we demonstrated novel function of Rae1 to prevent anoikis. Moreover, Rae1 localized not only NPC but also nucleaplasm where Rae1 potentially interacts with several epigenetic regulators such as Rad21 and HDAC2. Although additional future examination is required to validate the role of Rae1 in epigenetic regulations, current data indicated the novel functions of Rae1 in breast cancer.

Genomic DNA copy number aberration is frequently found in cancer and can contribute to cancer progression. Our genomic analysis in human breast cancers showed that Rae1 was freaquently amplified in breast cancer. Consistent with the genomic profiles, overexpression of Rae1 at protein levels was also observed in MCF7 cell line comparing to normal breast MCF10A cell line. The loss of function assay revealed that a silencing of Rae1 enhanced apoptosis upon loss of ancharage. Recent papers demonstrated that silencing of Rae1 expression in MCF-7 decreased migration/invasion ability without altering proliferation of cells. Taken together, these results indicate that targeting Rae1 functions may serve as promising therapeutic strategies for cancer treatment.

Accumulated evidence suggests that the Rae1 plays a role further than classical mRNA export pathways. Previous work related to mitosis suggested the link of Rae1 to microtubules, SMC1, and NuMA.

To counteract abnormalities of chromosomal segregation seen in cancer cells, the microtubule crosslinking valency of NuMA in mitotic spindles was regulated by Rae1. In contrast, Rae1 depletion induces defect in mitosis, forming the multipolar spindle cells and aberrant multinucleated cells. This sustainable events were than lead the cells to face apoptosis [23]. Notably, this report revealed that Rae1 localized in nucleoplasm and interacted with several epigenetic regulators. Therefore, how and whether Rae1 coodinate in genomic topology and functions should be examined in future studies.

Breast tissue comprises glandular epithelial cells that rather unique compare to non-glandular tissue as to preserve its "normality" the coordination of apoptosis. The polarization is a key factor to maintain the balance between cell differentiation, proliferation, as well as cell survival vs death. Recent *Drosophila* research has revealed that interrupting genes regulating cell polarity such as *Scrib*, *Dlg* and *Lgl*, provokes hyperplastic progression. Other study purposed that ErbB2 and/or c-Myc; an oncogene, induces both proliferation and apoptosis in mammary epithelia. Additionaly, overexpression of the anti apoptotic protein Bcl2, or loss of the pro-apoptotic protein Bax, can work together with Myc to support tumourigenesis. Therefore, the novel function of Rae1 to prevent anoikis would possibly be crucial during cancer progressions affecting polarity/morphogenesis [48].

I.6. CONCLUSION

We found that upregulated Rae1 is functionally involved in preventing anoikis, which is caused by novel role of Rae1 in nucleoplasm related to epigenetic regulation.

I.7. REFERENCES

[1] H. Sung, J. Ferlay, R. L. Siegel, M. Laversanne, Global Cancer Statistics 2020: GLOBOCAN Estimates of Incidence and Mortality Worldwide for 36 Cancers in 185 Countries, Ca Cancer J Clin. 71 (2021) 209–249.

[2] I. Phipps and C. I. Li, Breast Cancer Biology and Clinical Characteristics, Breast Cancer Epidemiology (2009) 21-46.

[3] R. G. Margolese, G. N. Hortobagyi, T. A. Buchholz, Breast Cancer Biology. In: Kufe DW, Pollock RE, Weichselbaum RR, et al., editors. Holland-Frei Cancer Medicine. 6th edition. Hamilton (ON): BC Decker (2003) Available from: https://www.ncbi.nlm.nih.gov/books/NBK13081/

[4] X. Dai, C. Hongye, B. Zhonghu, L. Jia, Breast Cancer Cell Line Classification and Its Relevance with Breast Tumour Subtyping, Journal of cancer 8(2017): 3131-3141.

[5] C. M. Perou, T. Sorlie, M. B. Eisen, et al., Molecular portraits of human breast tumours, Nature 406 (2000) 747–752.

[6] T. Sorlie, C. M. Perou, R. Tibshirani, et al., Gene expression patterns of breast carcinomas distinguish tumour subclasses with clinical implications. Proc Natl Acad Sci USA 98 (2001) 10869–10874.

[7] L. J. van't Veer, H. Dai, M. J. van de Vijver, et al., Gene expression profiling predicts clinical outcome of breast cancer, Nature 415 (2002) 530–536.

[8] M. J. van de Vijver, Y. D. He, L. J. van't Veer, et al., A gene-expression signature as a predictor of survival in breast cancer. New Engl J Med. 347 (2002) 1999–2009.

[9] T. Sorlie, R. Tibshirani, J. Parker, et al., Repeated observation of breast tumour subtypes in independent gene expression data sets, Proc Natl Acad Sci USA. 100 (2003) 8418–8423.

[10] P. Farmer, H. Bonnefoi, V. Becette, et al., Identification of molecular apocrine breast tumours by microarray analysis, Oncogene 24 (2005) 4660–4671.

[11] Z. Hu, C. Fan, D. S. Oh, et al., The molecular portraits of breast cancer are conserved across microarray platforms, BMC Genomics. 7 (2006) 96.

[12] W. Reed, V. A. Florems, R. Holm, et al., Elevated levels of p27, p21, and cyclin D1 correlate with positive oestrogen and progesterone receptor status in node-negative breast carcinoma patients, Virchows Arch. 435 (1999) 116–124.

[13] Y. L. Oh, J. S. Choi, S. Y. Song, et al., Expression of $p21^{Waf1}$, $p27^{Kip1}$ and cyclin D1 proteins in breast ductal carcinoma in situ: relation with clinicopathologic characteristics and with p53 expression and estrogen receptor status, Pathol Int. 51(2001) 94–99.

[14] G. Callagy, E. Cattaneo, Y. Daigo, et al., Molecular classification of breast carcinomas using tissue microarrays, Diagn Mol Pathol. 12 (2003) 27–34.

[15] T. Sorlie, C. M. Perou, R. Tibshirani, et al., Gene expression patterns of breast carcinomas distinguish tumour subclasses with clinical implications, Proc Natl Acad Sci USA. 98 (2001) 10869–10874.

[16] Molino, R. Micciolo, M. Turazza, et al., Ki-67 immunostaining in 322 primary breast cancers: associations with clinical and pathological variables and prognosis, Int J Cancer. 74(1997) 433–437

[17] Ruiz C, Seibt S, Al Kuraya K, Siraj AK, Mirlacher M, Schrami P et al (2006) Tissue microarrays for comparing molecular features with proliferation activity in breast cancer. Int J Cancer 118:2190–2194

[18] M. Raices, M. A. D'Angelo, Nuclear pore complex composition: a new regulator of tissue-specific and developmental functions, Nat Rev Mol Cell Biol. 13 (2012) 687-99.

[19] F. Alber, S. Dokudovskaya, L. M. Veenhoff, et al., The molecular architecture of the nuclear pore complex, Nature 450 2007) 695-701.

[20] A. Chadrin, B. Hess, M. S. Roman, et al., Pom33, a novel transmembrane nucleoporin required for proper nuclear pore complex distribution, J Cell Biol. 189 (2010) 795-811.

[21] D'Angelo, M. A. & Hetzer, M. W. Structure, dynamics and function of nuclear pore complexes. Trends Cell Biol. 18, 456–466 (2008).

[22] J.R. Babu, K.B. Jeganathan, D.J. Baker, et al., Rae1 is an essential mitotic checkpoint regulator that cooperates with Bub 3 to prevent chromosome missegregation, J. Cell Biol. 160 (2003) 341e353.

[23] R.W.Wong, G. Blobel, E. Coutavas, Rae1 interaction with NuMA is required for bipolar spindle formation, Proc. Natl. Acad. Sci. U.S.A. 103 (2006) 19783e19787.

[24] D. Kraemer, G. Blobel, mRNA binding protein mrnp 41 localizes to both nucleus and cytoplasm, Proc. Natl. Acad. Sci. U.S.A. 94 (1997) 9119e9124.

[25] R. W. Wong, Interaction between Rae1 and cohesin subunit SMC1 is required for proper spindle formation, Cell Cycle 9 (2010) 198e200.

[26] R.W. Wong, G. Blobel, Cohesin subunit SMC1 associates with mitotic microtubules at the spindle pole, Proc. Natl. Acad. Sci. U. S. A 105 (2008) 15441e15445.

[27] K.B. Jeganathan, D.J. Baker, J.M. van Deursen, Securin associates with APCCdh1 in prometaphase but its destruction is delayed by Rae1 and Nup98 until the metaphase/anaphase transition, Cell Cycle 5 (2006) 366e370.

[28] T. Funasaka, V. Balan, A. Raz, R.W. Wong, Nucleoporin Nup98 mediates galectin-3 nuclear-cytoplasmic trafficking, Biochem. Biophys. Res. Commun. 434 (2013) 155e161.

[29] T. Funasaka, H. Nakano, Y. Wu, C. Hashizume, L. Gu, T. Nakamura, W. Wang, P. Zhou, M.A. Moore, H. Sato, R.W. Wong, RNA export factor Rae1 contributes to Nup98-HOXA9-mediated leukemogenesis, Cell Cycle 10 (2011) 1456e1467.

[30] Y. Ren, H. S. Seo, G. Blobel, A. Hoelz, Structural and functional analysis of the interaction between the nucleoporin Nup98 and the mRNA export factor Rae1, Proc. Natl. Acad. Sci. U.S.A. 107(2010) 10406-11.

[31] X. Zheng, X. Zhao, Y. Zhang, et al., Rae1 promotes BMAL1 shuttling and regulates degradation and activity of CLOCK: BMAL1 heterodimer, Cell Death Dis. 10 (2019) 62.

[32] J.H. Oh, J.Y. Lee, S. Yu, et al., Rae1 mediated ZEB1 expression promotes epithelial-mesenchymal transition in breast cancer, Sci. Rep. 9 (2019) 2977.

[33] Y. Cheng, C. He, M. Wang, et al., Targeting epigenetic regulators for cancer therapy: mechanisms and advances in clinical trials. Sig Transduct Target Ther. 4 (2019) 62.

[34] O. Witt, H. E. Deubzer, T. Milde, I, Oehme: HDAC family: what are the cancer relevant targets? Cancer Lett. 277(2009) 8-21.

[35] P. A. Marks: Histone deacetylase inhibitors: a chemical genetics approach to understanding cellular functions. Biochim Biophys Acta. 1799 (2010) 717-725.

[36] K. T. Smith, J. L. Workman, Histone deacetylase inhibitors: anticancer compounds. Int J Biochem Cell Biol. 41(2009) 21-25.

[37] F. Gharahdaghi, C. R. Weinberg, D. A. Meagher, et al., Mass spectrometric identification of proteins from silver-stained polyacrylamide gel: A method for the removal of silver ions to enhance sensitivity, Electrophoresis 20 (1999) 601-605.

[38] C. Chen, J. hou, J. J Tanner, J. Cheng, Bioinformatics Methods for Mass Spectrometry-Based Proteomics Data Analysis, Int. J. Mol. Sci. 21 (2020) 2873.

[39] A. Fabregat, K. Sidiropoulos , G. Viteri, et al., Reactome pathway analysis: a highperformance in-memory approach, BMC bioinformatics 18 (2017) 142.

[40] G. Prelich, Gene Overexpression: Uses, Mechanisms, and Interpretation, Genetics, Vol. 190 (2012) 841–854

[41] J.H. Oh, H. Hur, J. Y. Lee, et al, The mitotic checkpoint regulator Rae1 induces cancer cell phenotypes by mediating epithelial-mesenchymal transition. Sci. Rep. 7 (2016) 42256.

[42] Y. Kobayashi, T. Masuda, A. Fujiii, et al, Mitotic check point regulator Rae1 promotes tumour growth in colorectal cancer.

[43] K. Chin, S. DeVries, J. Fridlyand, et al., Genomic and transcriptional aberrations linked to breast cancer pathophysiologies, Cancer Cell **10** (2006) 529-41.

[44] M. A. Moore, A cancer fate in the hands of a samurai. Nat Med. **16** (2010) 963-5.

[45] M. A. Moore, K.Y. Chung, M. Plasilova, et al., Nup98 dysregulation in myeloid leukemogenesis. Ann N Y Acad Sci. **1106** (2007) 114-42.

[46] P. Marina, D. Mitchell, S. Ian, Studies of apoptosis in breast cancer, BMJ 322 (2001)1528–32

[47] R. W. Wong, G. Blobel, E. Coutavas, Rae1 interaction with NuMA is required for bipolar spindle formation. Proceedings of the National Academy of Sciences 103 (2006) 19783-19787.

[48] L. Zhan, A. Rosenberg, K.C. Bergami, et al., Deregulation of scribble promotes mammary tumourigenesis and reveals a role for cell polarity in carcinoma, Cell 135 (2008) 865-78.

[49] T.O. Tolsma, J.C. Hansen, Post-translational modifications and chromatin dynamics. Essays Biochem. 63 (2019) 89–96.

CHAPTER II. Rae1 in viral disease: Overexpression of SARS-CoV-2 protein Orf6 dislocates Rae1 and Nup98 from the nuclear pore complex

II.1. ABSTRACT

SARS-CoV-2, a new human betacoronavirus, has produced an immense outbreak worldwide since December 2019 . Relationships between SARS-CoV-2 viral proteins and nucleoporins (Nups) of infected host have been proposed in several research, although their roles are yet unclear. We showed here that the open-reading frame 6 (Orf6) of SARS-CoV-2 may directly control localization and function of Nup. The Orf6 protein impaired nuclear rim staining of Rae1 and Nup98, according to our findings. As a result of the disturbance, abnormal nucleocytoplasmic trafficking occurred, resulting in nuclear accumulation of mRNAtransporters such hnRNPA1. The size of the nucleus of the host cell was eventually decreased, and cell development was inhibited.

Keywords: SARS-CoV-2, Rae1, Orf6, hnRNPA1

II.2. INTRODUCTION

II.2.1. Covid 19 and the characteristic of SARS-CoV-2

The severe acute coronavirus respiratory syndrome coronavirus-2 (SARS-CoV-2) is a positive-sense single-stranded RNA virus that caused a life-threatening disease known as COVID-19 [1]. Firstly reported in December 2019, SARS CoV-2 has just been growing and expanding rapidly, creating global pandemic and generating enormous worldwide concern [2]. There is effectively no proven therapy for COVID-19, with supportive and symptomatic care as the main therapies thus far [3]. An alarmingly rapid increase in new fatalities has compelled experts all around the world to establish effective vaccinations and/or treatment programs that inhibit infection with or replication of SARS-CoV-2. Many unanswered questions concerning the molecular invasion and replication routes of SARS-CoV-2 components, indeed, create barriers for COVID-19 research. The non-biased methodology in proteomic study to molecularly analyze infected cells may serve as an effective tool to identify the pathogenesis of viruses and; hereinafter, the possible therapeutic targets

Previous study has isolated the virus from bronchoalveolar-lavage (BAL) samples taken from individuals suffered from severe pneumonia followed by performing metagenomic RNA sequencing. The result has identified a betacoronavirus as the causative agent of this disease. They revealed close similarity of the sequences to SARS-CoV (79.6% identical) [4]. The genomic size SARS-CoV-2 is 29.9 kb and encodes 28 confirmed proteins. The genome included open reading frame (orf) 1a/b, which is the biggest viral gene by far, flanked by 5'- untranslated region (5'- UTR). The orf encoding polyproteins Orf1a and Orf1ab, splitting into non-structural protein 1-16, that make up the complex of viral transcription/replication. The complexes are papain-like proteinase (PL^{pro}; Nsp3), RNA-dependent RNA polymerase (RdRp,Nsp12 in complex with Nsp7-Nsp8 heterodimer co-factor), nucleoside triphosphate hydrolase (NTPase) and helicase (Nsp13) [5], exonuclease (Nsp14), endoribonuclease (NendoU,Nsp15), and RNA 5′ cap structure (Nsp14 combined

with the Nsp16-Nsp10 methyltransferase complex). The nucleocapsid (N), membrane (M), envelope (E), and spike (S) (**Figure 10)** are the primary properties of SARS-CoV-2 structural proteins encoded by genes of 3′ end untranslated region (3'-UTR) from the remaining viral genome. Eight accessory proteins such as Orf3a and b, Orf6, Orf7a and b, Orf8, Orf9b and Orf10, are presented here as well. The above mentioned accessory proteins functions remain poorly understood most likely due to inadequately-defined domain structures. However, previous finding may indicated the extensive host proteins interaction with those accessory proteins to promote the replication and growth of the viruses [6].

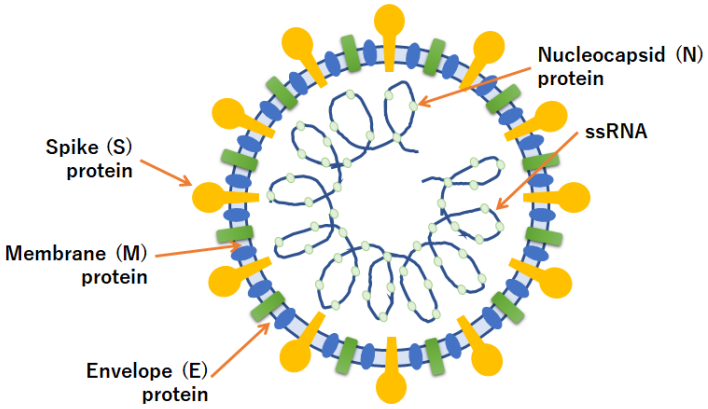

Figure 10. Illustration of structural feature of SARS-CoV2 with its primary proteins.

II.2.2. Nuclear Pore Complex in viral diseases

Each of virus categories including DNA and RNA genome face the Nuclear Pore Complexes (NPCs) in a different manner to cause the disease. NPCs consist of about thirty different types of Nup, formed by an eight-fold symmetric central scaffold, eight cytoplasmic filaments, and eight nucleoplasmic filaments (nuclear basket), with the pores presenting rotational symmetry [7-12]. Many Nups contain Phenylalanine-glycine (FG) repeats with its dynamic hydrophobic interactions among of them in the central scaffold create a cohesive meshwork that can make the NPC become a selective channel [13,14].

Viruses with DNA genetic material, need to travel along the NPC after passing through the cytoplasm, to access the nucleus and further fusing their genes with the host cell to enable proliferation. They generate more complicated activities, such as the nuclear import of a viral genome and the nuclear export of a newly synthesized viral genomic RNA to the cytoplasm. Meanwhile, proliferation of RNA viruses occured in the cytoplasm inside of their host, without entering the nucleus. However, they tend to hijack the host nuclear transport for suppressing the interferon (IFN)-inducing antiviral responses. Moreover, cells infected by these RNA viruses undergo NPC structural and functional nucleocytoplasmic disorder. This will leave the possibility for the various host proteins to become jammed in the cytoplasm. Most likely, as export and import activities persist upon cell infection, the ongoing events regarding to NPC remains an issue [15-18].

The classical import pathway utilizes the heterodimeric importin-α/β1 transport receptor, in which importin-α works as an adaptor protein, bringing its cargo in concert with importin-β to translocate it into the nucleus. The conserved N-terminal autoinhibitory importin-β-binding (IBB) domain and the C-terminal Armadillo (Arm) repeats (the NLS-binding sites) of α-importins are important for the nuclear import of the NLS-bearing cargo [19-24].

II.2.3. Rae1-Nup98 regulation after viral infection

Recent study has identified more than thousands virus-host protein-protein interactions in HEK293T cell lines. Interaction of SARS-CoV-2 with host was mapped based on their epitope-tagged viral proteins resulted from immunoprecipitation pairing with mass spectrometry [25,26]. There, several nups (NUP 210, NUP214, and Nup98) have been found to interact with SARS-CoV-2 protein. Reportedly, Nup98 exhibited to bind with Ribonucleic acid export 1 (Rae1) as Nup98/Rae1 complex. Particularly, the Orf6 interacts with the complex as depicted in **Figure 11** [25].

Additionaly, the phosporylation of Nup98 was recognized to augment at S888, where the peptidase domain located. Autocatalytic cleavage of this Nup is

essential to assemble into NPC; therefore interaction of Nup98-Orf6 may potentially hinders the export of host mRNA via NPC [25,27].

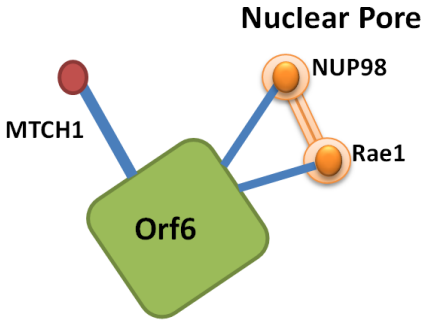

Figure 11. Illustration of Interaction of Orf6 of SARS-CoV-2 with protein complex (Nup98-Rae1).

Several pathways mediate mRNA export, and the Nxf1-dependent pathway is the dominant pathway for exporting bulk mRNAs [28-30]. In an Nxf1-dependent mRNA export, mature mRNAs are packaged into messenger ribonucleoprotein particles (mRNPs) that then recruit mRNA export factors (e.g., an Nxf1–Nxt1 heterodimer) [31,32]. The interaction between an Nxf1–Nxt1 heterodimer, Rae1, and Nup98 enables mRNA to be delivered to the cytoplasm [31]. the Nxf1-Nxt1 heterodimer most frequently requires dedicated export adaptors, including Aly/REF and UP56 [32].

In the HEK293T cell line, Orf6 binds to importin-α1 to further block the nuclear translocation of IRF3, resulting in an impaired production of type I IFN [33]. Other study using SARS-CoV-2-infected Vero E6 cells reported that type I and type II IFNs failed to induce the transcription of IFN-stimulated genes (ISGs) upon an obstacle of the STAT1 and STAT2 nuclear translocation by Orf6. SARS-CoV-1 Orf6 acts as an IFN-antagonist; it binds to importin-α1 and tethers importin-β1 to the endoplasmic reticulum (ER)/Golgi membrane, sequestrating the exportins (NTRs) from activated Signal Transducer And Activator Of Transcription 1 (STAT1) (pY-STAT1), thus blocking the nuclear translocation of a pY-STAT1 [33,34]. Two mechanisms have been proposed to elucidate this blockade. First, Orf6 binds to Nup98 via its C-terminal domain to interfere the

docking of cargo–importin-α5/β1 ternary complexes at the NPCs. The Orf6–Nup98 interaction does not affect the Nup98–Rae1 interaction, which suggests that Orf6 binding to Nup98 targets only the nuclear import pathway. Second, Orf6 competes with STAT1 and STAT2 for α-importins (α5 and α1) to block the STAT1/2 nuclear entryway. Nevertheless, these α-importins may not be the direct key players because their overexpression failed to rescue an Orf6-dependent blockade of green fluorescent protein (GFP)-tagged STAT1 nuclear import. The SARS-CoV-2 Orf6 interactions with Nup98 and Rae1; impressively, were much stronger than those of SARS-CoV-1 Orf6, implying the strong IFN antagonism triggered by SARS-CoV-2 contributes to the high prevalence of asymptomatic cases of SARS-CoV-2 infection [35].

In vesicular stomatitis virus (VSV), Rae1-Nup98 complex are also served as a pivotal target of the matrix protein (M) virus. heterogeneous ribonucleoprotein A1 (hnRNPA1) is relocalized by VSV in a Rae1-dependent fashion, which is not unpredicted given that hnRNPs are considered to function as mRNA export factors [19,38]. The C-terminal region of Orf6 contains a methionine, which is similar to VSV, and may help to interact with Rae1 and Nup98. With the exception of HIV capsid accessing the nuclear pore [20,21], it's unclear why SARS-CoV2 Orf6 needs Nups to interact with, even after infection. SARS-CoV2 exploits the host cell's protein-making machinery to convert the viruses' RNA into new copies one. We figured out that overexpression of GFP-Orf6 promoted Rae1 and Nup98 mislocalization. Also, we discovered that Orf6-transfected cells had significantly smaller nuclei, presumably because of hnRNPA1 nuclear accumulation and consecutive mRNA export delayed. Finally, we demonstrated that overexpression of Rae1 slightly ameliorated this condition.

II.3. MATERIALS AND METHODS

II.3.1. Plasmid and siRNA

Using EcoRI and BamHI restriction sites, constructs for overexpressing SARS-CoV-2 Orf6 were designed by ligating synthetic DNA into the pEGFP-N1 vector. The FLAG-Rae1 plasmid has been described before [39]. Stealth RNAi targeting Rae1 was generated to target the sequence corresponding to nucleotides 343-367 of human Rae1 mRNA (SIC001) bought from Sigma-Aldrich for Rae1 siRNA. The manufacturers of each materials are as described in the reference paper.

II.3.2. Cell culture and transfection

As previously described [40], HEK293T were grown in DMEM supplemented with fetal bovine serum for 10% (v:v) and penicillin-streptomycin with concentration of 50 U/mL. Cells were incubated at 37°C with 5% CO2. As previously described [41], transfection of DNA was carried out in 6-well plates by adding Lipofectamine 2000 with plasmid DNA or siRNA (1000 ng and 50 nM) respectively for each well based on manufacturer's procedure. The manufacturers of each materials for cell culture and transfection are as described in the reference paper.

II.3.3 Antibodies

Anti-beta actin, anti-GFP, anti-FLAG, anti-Rae1, anti-Nup98, anti-TPR, anti-NUP153, anti-Lamin B1, and anti-hnRNPA1 were used as primary antibodies for immunocytofluorescence, immunoprecipitation, and immunoblotting. Alexa fluor 488 goat anti-rabbit, alexa fluor 488 goat antimouse, rhodamine red goat anti-rabbit, rhodamine red goat anti-mouse, alexa fluor 633 goat anti-mouse, HRP-linked anti-rabbit IgG, HRP-linked anti-rat IgG, and horseradish peroxidase

(HRP)-linked anti-rabbit IgG, were used as secondary antibodies. The manufacturers of each antibodies are as described in the reference paper.

II.3.4. Immunostaining and super-resolution imaging

The 6-well plates equipped by glass coverslips were prepared to culture HEK293T. Cells on coverslips were then washed with PBS and fixed for 30 minutes with 4% paraformaldehyde in PBS. The washing step with PBS was repeated, and cells were permeabilized with 0.3% Triton X-100 in PBS for 3 minutes. Cells were washed again before blocked in PBS with 4% BSA at room temperature for 30 minutes. Incubation overnight of the coverslips were performed in 4% BSA/PBS supplemented with primary antibodies at dilution of 1:500. Next, cells were rinsed and the incubation with secondary antibodies were performed in 4% BSA/PBS at dilution of 1:500 dilution at room temperature for 2 hours. After PBS washing, The surface of coverslips with cells was then attached on slides and mounted by ProLong Diamond Antifade reagent with DAPI. The observation was performed using confocal laser-scanning microscope with 60X PlanApo/1.45NA DIC objective, as previous protocol [42]. The manufacturers of each materialsfor immunofluorescnence are as described in the reference paper.

II.3.5. Protein extraction and western blotting

To extract the protein, 100 µl lysis buffer + protease inhibitor cocktail (EDTA free) was used to disrupt 6 x 10^5 cells. The lysates were centrifuged at 14.000 x g at 4 ^oC for 10 minutes to obtain supernatants which were then separated using SDS PAGE and followed by gel transfer using PVDF membranes. The membranes were then incubated overnight by primary antibody and secondary HRP-conjugated antibodies, subsequently. Using the suitable HRP substrate, the proteins were detected via chemiluminescence. To capture the images, a LAS-4000 image analyzer was utilized. As previously described

[40,42], analysis for nuclear and cytoplaspic fraction was conducted as suggested by manufacturer. Thereafter, immunoblotting was used to examine cytoplasmic and nuclear extracts. The manufacturers of each materials for protein extraction and western blotting are as described in the reference paper.

II.3.6. Immunoprecipitation (IP)

The transient transfection was performed using pEGFP-Orf6 and/or FLAG-Rae1 plasmids. Following the collection of cells post 48 hours of transfection, cells were then centrifuged at 500 x g for 5 minutes and disrupted by lysis buffer + protease inhibitor cocktail (EDTA free). To obtain the supernatants, cells were centrifuged at 14.000 x g for 10 minutes, then antibodies for specific purposes (5 µg) and Dynabeads protein A/G were added to the supernatants. The samples were then rotated at 4 ^{o}C for overnight incubation time. On the subsequent day, the beads were washed using lysis buffer and repeat for 3 times. Immunoblotting was used to examine whole-cell lysates and immunoprecipitates, as previously reported [42]. The manufacturers of each materials for IP are as described in the reference paper.

II.3.7. Cell proliferation assay

Cells with a density of $3x10^3$ cells per well were plated and incubated into 96 wells plates for the specified period. The MTT technique was used to determine cell viability. Specifically, every wells were added by 10 µL of MTT, followed by 3 hours incubation and 100 µL stop solution to terminate the reaction. The 570 nm absorbancy was used to measure the samples after they had been properly mixed. The manufacturers of each materials for MTT assay are as described in the reference paper.

II.3.8. Nuclear size measurement

Measurements of nuclear region and intensity were standardized to controls. For independently repeated experiments, averaging and statistical analysis were conducted [44]. To determine statistical significance, GraphPad PRISM 7 software was used to run a two-tailed Student's T-test assuming equal variances. The figure legends include P-values, the number of separate experiments, the number of nuclei quantified, and error bars.

PRISM 7 software was used for statistical analysis. The mean and standard deviation are used to present the data. Student's t-test or one-way ANOVA analysis were used to see if there were statistically significant differences in mean or median values across groups. A statistically significant difference was defined as a P value of less than 0.05.

II.4. RESULTS

II.4.1. Orf6 of SARS-CoV-2 overexpression dislocated Rae1 from the nuclear envelope.

We postulated that several forms of Rae1 and that Orf6 protein interacts with Rae1 might exsisted in a spatiotemporal manner considering that Rae1 can be found in the nuclear membrane, nucleoplasm, and cytoplasm. This interaction may also generate different Orf6-Rae1 protein complexes involved in host gene reticence. We transfected HEK293T cell line with Orf6 which was constructed into GFP-fluorescence, and provided the experimental control by GFP vector to confirm their interaction (**Figure 12. A**). In **Figure 12.B**, Orf6 interacts unequivocally with Rae1, instead of other nucleoporins like TPR as well as NUP153. This result was obtained after performing immunoprecipitation from co-transfection of GFP-Orf6 and FLAG-Rae1 lysates in HEK293T cell line.

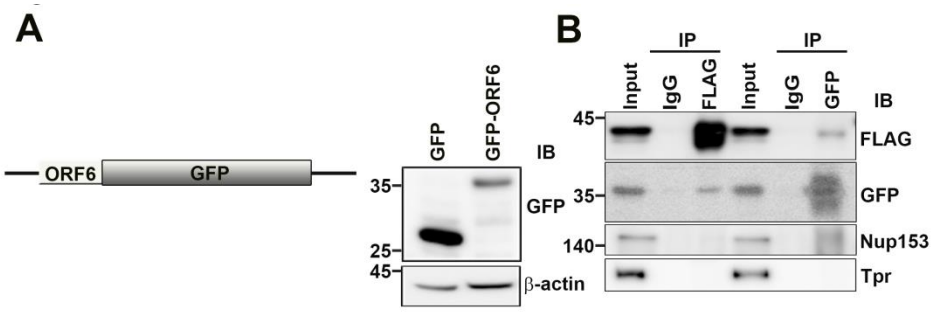

Figure 12.A. Schematic design of Orf6 fused with GFP (pEGFP-Orf6), and its protein expression by western blotting. **B**. Protein expression level of immunoprecipitated HEK293T previously co-transfected with pEGFP-Orf6 and FLAG-Rae1. Anti-GFP, anti-FLAG, and rabbit IgG were applied for immunoprecipitation, and additionally anti Nup153 and TPR for protein detection.

These findings are in line with newest data from IPMS and BioID-based interactome studies [25,45]. Confocal microscopy was used to analyze localization of Rae1in cells overexpressed with Orf6. Orf6 overexpression caused Rae1 to be displaced from the nuclear envelope to the cytoplasm in both HEK293T (**Figures 13.A** and **B**) and the human lung cancer cell line PC9 (**Figure 13.C** and **D**). These findings show that changes in Rae1 distribution are linked to disruptions in mRNA nucleocytoplasmic transport proteins associated to Rae1 function and the suppression of host gene expression by SARS-CoV-2 Orf6. In Orf6-transfected cells, we also saw a reduction in nuclear size relative to controls [**Figure 14.A** (n 14 50)].

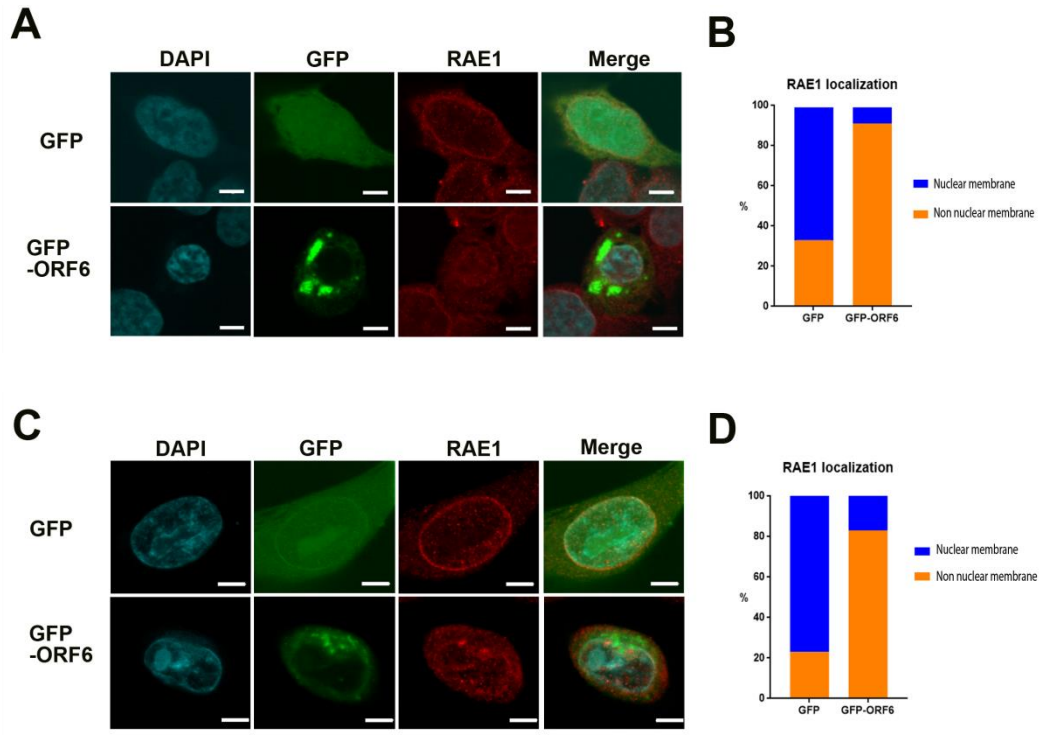

Figure 13. Localization of GFP and Rae1 in HEK293T (**A**) and PC9 **(C)** by confocal imaging (scale bars are 5µm). The cells were transfected with pEGFP-N1 or pEGFP-Orf6. GFP, anti Rae1, and chromatin are shown by green, red, and blue color respectively. **B,D**. Quantification of localization signal of Rae1 in nuclear and cytoplasmic in HEK293T cells **(B)** (n=57 for both pEGFP-N1 and pEGFP-Orf6 transfection) and PC9 cells **(D)** (n=43 for pEGFP-N1 and n= 58 for pEGFP-Orf6 transfection)**.**

As depicted in **Figure 14.B**. montages of representative DAPI-stained nuclei indicated Orf6 overexpression that led to reduced nuclear size. These findings reveal that changing Orf6 levels influences the location of the NPC protein Rae1, implying that variations in nuclear RNA export capacity are responsible for inspected changes in nuclear size.

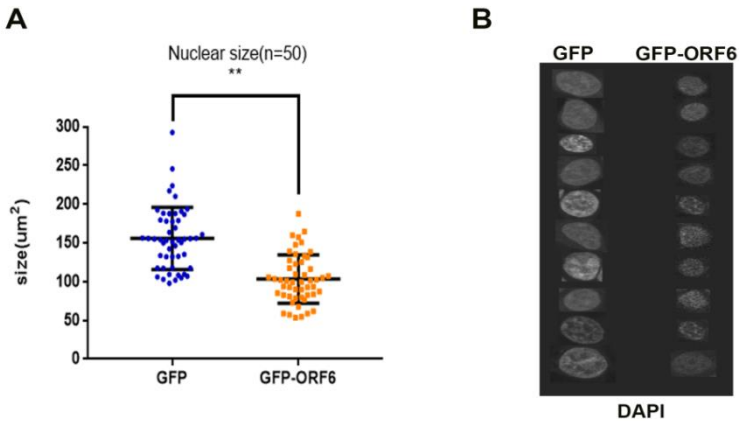

Figure 14. A. Comparison of nuclear size reduction of GFP and GFP-Orf6. **B**. montages of representative DAPI-stained nuclei

II.4.2. Orf6 of SARS-CoV-2 overexpression promoted the dislocation of Nup 98 from the nuclear envelope

We then used coimmunofluorescence labeling to look at the Rae1 binding partner Nup98. In comparison to GFP vector control cells, GFP-Orf6 overexpression caused Nup98 to be displaced from the nuclear membrane to the cytoplasm in HEK293T cells as seen in **Figure 15.A** and **B** (n = 70) and PC9 cells (**Figure 15.C** and **D)** (n = 54 and 21, respectively).

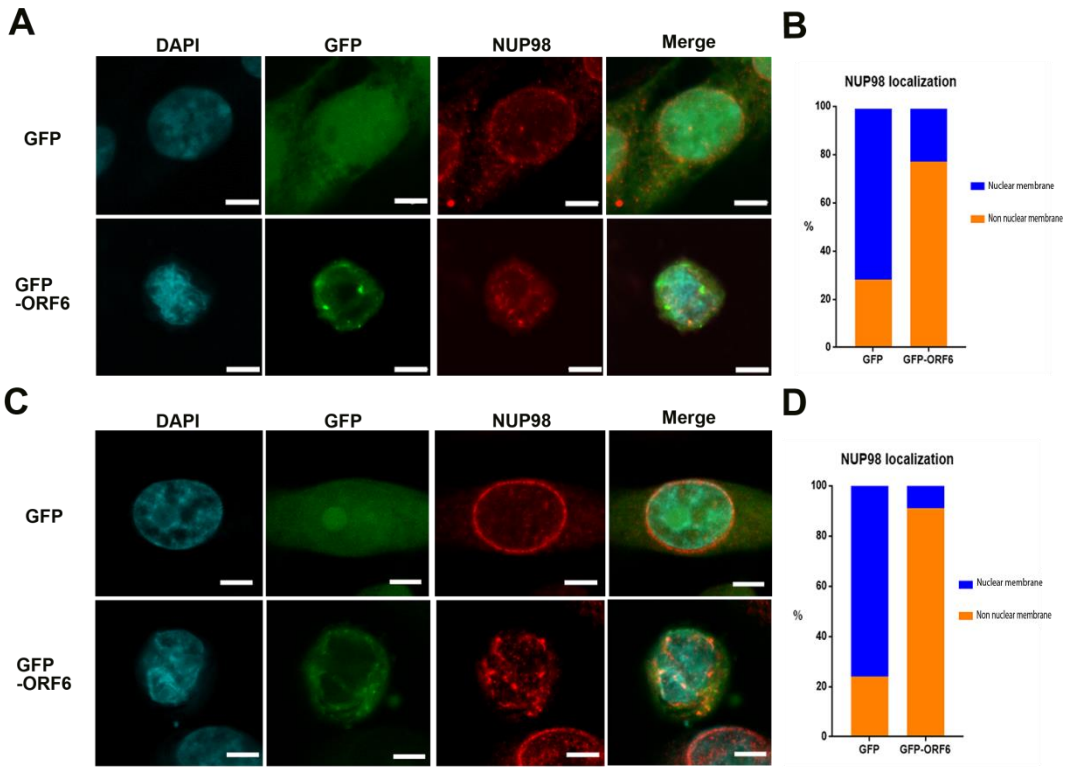

Figure 15. Nup98 (not lamin B1) localization was altered by Orf6 of SARS-CoV-2. Localization of GFP and Rae1 in HEK293T (**A**) and PC9 **(C)** by confocal imaging (scale bars are 5µm) with pEGFP-N1 or pEGFP-Orf6 were transfected into the cells. GFP, anti Nup98, and chromatin are shown by green, red, and blue color respectively. **B, D**. Quantification of localization signal of Nup98 in nuclear and cytoplasmic in HEK293T cells **(B)** (n¼ 70 for both pEGFP-N1 and pEGFP-Orf6 transfection) and PC9 cells **(D)** (n ¼ 54 for pEGFP-N1 and n ¼ 21 for pEGFP-Orf6 transfection)**.**

Furthermore, immunoblotting tests revealed that Orf6 overexpression altered Rae1 and Nup98 protein levels (**Figure 16.A)**. On the staining of nuclear membrane, Orf6 overexpression showed no influence, since it preserved its punctate distribution, according to double labeling with Lamin B1, a nuclear membrane marker (**Figure 16.B**). These findings show that even only with expression of Orf6 is enough to disrupt the nucleocytoplasmic mRNA transport factors Rae1 and Nup98, resulting in mislocalization of the host endogenous mRNA export machinery and, as a result, a reduction in nuclear size.

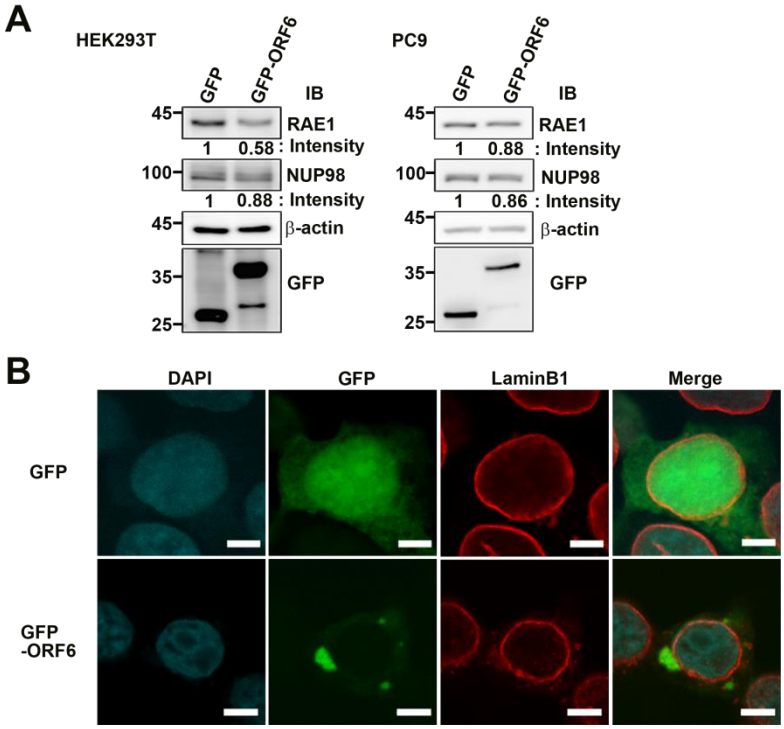

Figure 16. A. Protein level of Rae1 and Nup98 by western blotting in HEK293T and PC9, transfected by pEGFP-Orf6. **B**. localization of GFP and lamin B1 in HEK293T cells by confocal imaging with pEGFP-N1 or pEGFP-Orf6 were

transfected into the cells. GFP, anti lamin B1, and chromatin are shown in green, red, and blue respectively. Scale bars are 5μm

II.4.3. Orf6 of SARS-CoV-2 overexpression strongly accumulates hnRNPA1 signal in nucleus

In the multiple phase of mRNAs export, first mRNAs need to be packaged into messenger ribonucleoprotein particles (mRNPs), followed by transportation across NPCs, and remodeling activities of mRNP upon the translation. Therefore, expression and localization of hnRNPA1 need to be observed. hnRNPA1 is normally associated to RNAs in both nucleus and some cytoplasmic mRNAs, throughout their processing. The NPC that experiences the changes of dynamic in structure and function following transportation, is considered to chaperone mRNAs via hnRNPA1-containing mRNPs. Notably, hnRNPA1 relocalization after VSV infection was previously linked to VSV-induced gene suppression and shown to have dependency to the host factor Rae1 [19]. By changing Rae1 localization, we wanted to see if Orf6 spatiotemporally influenced hnRNPA1 subcellular distribution. To designate the nuclear compartment, HEK293T with GFP-Orf6 transfection were stained with DAPI. Furthermore this transfected cells were also tagged with an anti hnRNPA. **In Figure 17.A**, the top row for each protein shows mock-transfected GFP vector control samples, while the bottom row shows GFP-Orf6-transfected cells.

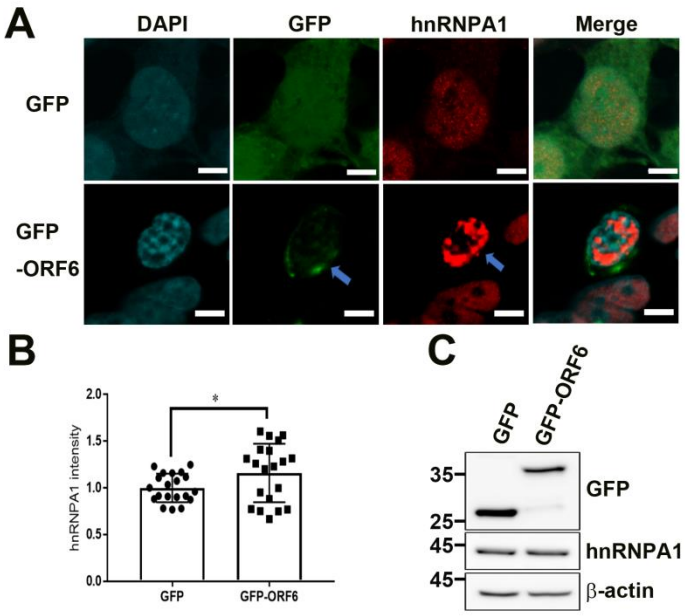

Figure 17. Accumulation of hnRNPA in the nucleus following Orf6 overexpression which hijacked Rae1 function. **A**. Localization of GFP and hnRNPA1 in HEK293T cells by confocal imaging with pEGFP-N1 or pEGFP-Orf6 were transfected into the cells. GFP, anti hnRNPA1, and chromatin are shown in green, red, and blue respectively. Scale bars are 5μm. **B.** Quantification of localization signal of hnRNPA in nuclear HEK293T cells following pEGFP-N1 or pEGFP-Orf6 transfection (n ¼ 20, respectively). Unpaired t-test was performed using GraphPad QuickCalcs. *p < 0.05. **C** hnRNPA1 protein level by western blotting in HEK293T cells with GFP-Orf6 transfection.

The hnRNPA localization coincided with DAPI in control cells, suggesting the intranuclear signal of hnRNPA. Here, the Orf6 overexpression only was not sufficiently shifted the hnRNPA1 to the cytoplasm, according to our findings. In GFP-Orf6-transfected cells, the fluorescence signal from hnRNPA1 was dramatically enhanced and persistantly stayed inside the nuclear region. This finding also suggests that Orf6 overexpression caused hnRNPA1 to deposit inside the nucleus. Furthermore, if the imaging datas described above are true, some part of Rae1 siRNA overexpression would mirror the GFP-Orf6 phenotype, such as the repeat occurence of aberrant hnRNPA1 nuclear accumulation. Obviously, confocal imaging (**Figure 18.A**) and a biochemical fractionation experiment (**Figure 18.C** and **D**) of Rae1-knockdown HEK293T cells demonstrated that

hnRNPA1 protein levels were essentially unaffected and that hnRNPA1 was continuously stacked in the nucleus.

Accordingly, if our idea is accurate, the GFP-Orf6 and FLAG-Rae1 overexpression, in some part would alleviate accumulation of hnRNPA1 via sequestration of endogenous nuclear hnRNPA1. Consistent with our prediction, we found that hnRNPA1 nuclear accumulation was partially relieved by hnRNPA1 nuclear stacking (**Figure 18.C** and **D**).

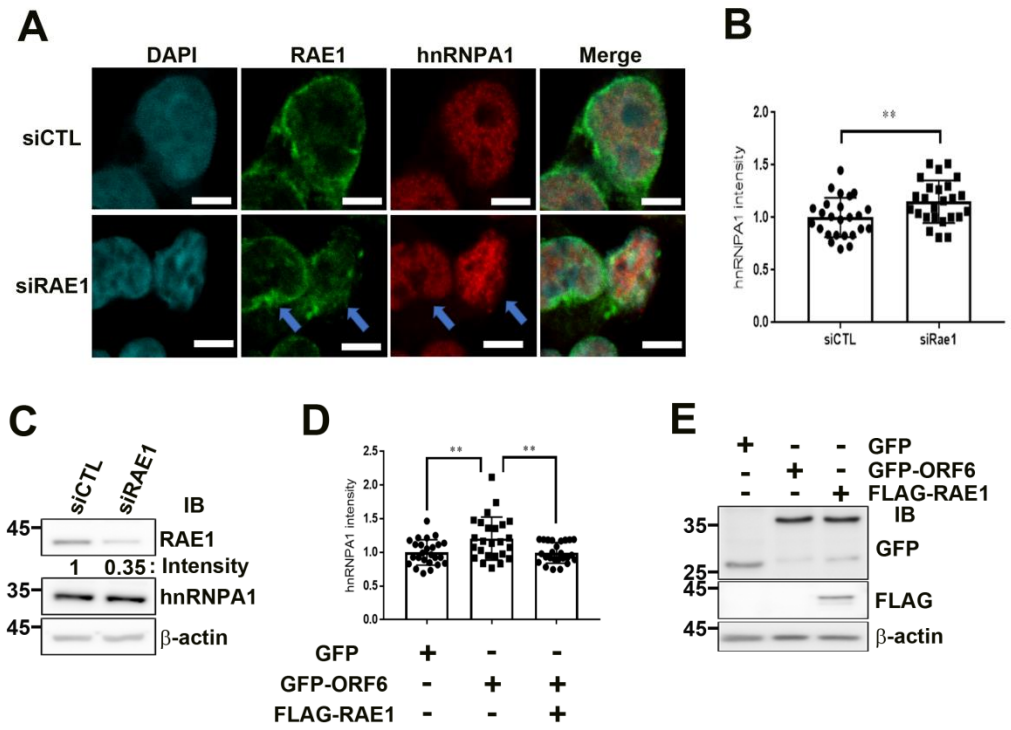

Figure 18. **A**. Localization of Rae1 and hnRNPA1 in HEK293T cells by confocal imaging with Rae1 siRNA were transfected into cells. GFP, anti hnRNPA1, and chromatin are shown in green, red, and blue respectively. Scale bars are 5μm. **B.** Quantification of localization signal of hnRNPA in nuclear HEK293T cells following control or Rae1 siRNA transfection (n ¼ ¼ 25 per group). Unpaired t-test was performed using GraphPad QuickCalcs. **p < 0.01. **C** Rae1 and hnRNPA1 protein level by western blotting in HEK293T cells with control or Rae1 siRNA transfection. **D.** Quantification of localization signal of hnRNPA in nuclear HEK293T cells following GFP or GFP-Orf6 transfection or GFP Orf6 and FLAG-Rae1 co-transfection (n ¼ 25 per group). Dunnett's multiple comparisons test was performed using GraphPad QuickCalcs. **p < 0.01. **E.** GFP and FLAG protein level by western blotting in HEK293T cells with pEGFP-N1 or pEGFP-Orf6 transfection, or pEGFP-Orf6 and FLAG-Rae1 co-transfection.

Cell proliferation inhibition was also partially rescued (**Figure 19**). As a result, a highly feasible interpretation of our results is that FLAG-Rae1 binds to endogenous hnRNPA1 and sequesters it.

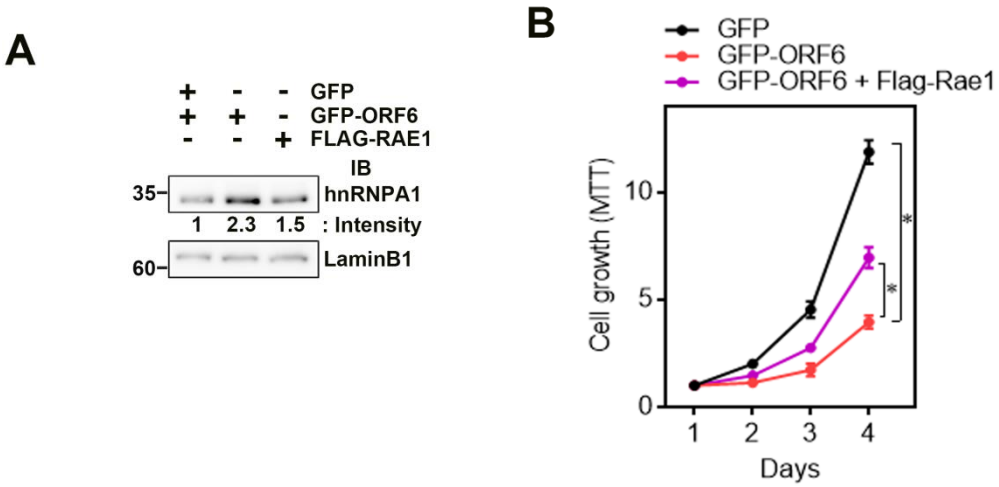

Figure 19. A. Protein level of Hela transfected by GFP-Orf6 and/or FLAG-Rae1 by westernblotting. **B**. Cell proliferation by MTT assay

II.5.DISCUSION

In this paper, we show evidence that the Orf6 of SARS-CoV-2 might vital for proliferation of virus through the displacement of Nup Rae1 and Nup98. The entrance of Orf6 into cells triggers a chain of molecular and cellular reactions, according to our findings. The Orf6 of SARS-CoV-2 is thought to sabotage the host mRNA export mechanism. By modulating hnRNP trafficking dynamics, Orf6 of SARS-CoV-2 seems to hijack Nup98 and Rae1 NPC protein from the host to further inhibit the translation events. the NPC proteins hijacking might be an example of the critical mechanism resulting in COVID-19.

We used the Adaptive Poisson-Boltzmann Solver in PYMOL (http://pymol.org) to perform electrostatic mapping. We also ran simulations of two other predicted Orf6 three-dimensional configurations. Furthermore, using high-speed atomic force microscopy, we have devised a nanoscopic approach to view the docking of individual influenza virus proteins to exosomes [30-33]. It is

supposed to be advantageous in forthcoming study to observe the dynamical protein of Orf6 and NPC, real time.

Interferon antagonists encoded by SARS-CoV-2 decelerate host cell immune response to 1.) identify the infection, 2.) sense and conduct signaling pathway and 3.) express the genes in response to interferon stimulation [46]. Orf6 is also thought to have a function in the hosts innate immunity [36, 47,]. The main property of antiviral response in innate immunity of the host is considered the interferon, specifically type I. A study of SARS-CoV-2 viral proteins by Li and colleagues discovered that the type I interferon signaling pathway potential inhibitors were nucleocapsid, Orf6, and Orf8 viral protein. Orf6 supresses the production of type I interferon as well as the downstream signalling activity, according to Lei et al. [48]. The crucial antagonist action of Orf6 is specified by the region in Carboxy-terminus. Proteins encoded by several pathogenic RNA viruses are able to selectively oppose nuclear import in blocking host innate immunity and other essential cellular functions in order to promote viral replication and transmission within hosts [49]. As an example, L-protein in some cardiovirus may have direct interaction with Ran-GTPases, that are necessary in exporting the nuclear mRNA [50,51]. Similarly, the VP24 of Ebola virus links to karyopherin-α1 and prevents STAT1 from entering the nucleus [52]. However, it is still important to be investigated whether Orf6's regulation of host innate immunity is linked to the dislocation of Rae1 and Nup98 and the reduction of nuclear size.

II.6. CONCLUSION

The Orf6 of SARS-CoV-2 has the ability to displace the Rae1 and Nup98 complex from its main origin, resulting the disturbance of nucleocytoplasmic trafficking and eventually the accumulation of mRNAtransporters like hnRNPA1 (**Figure 20)**

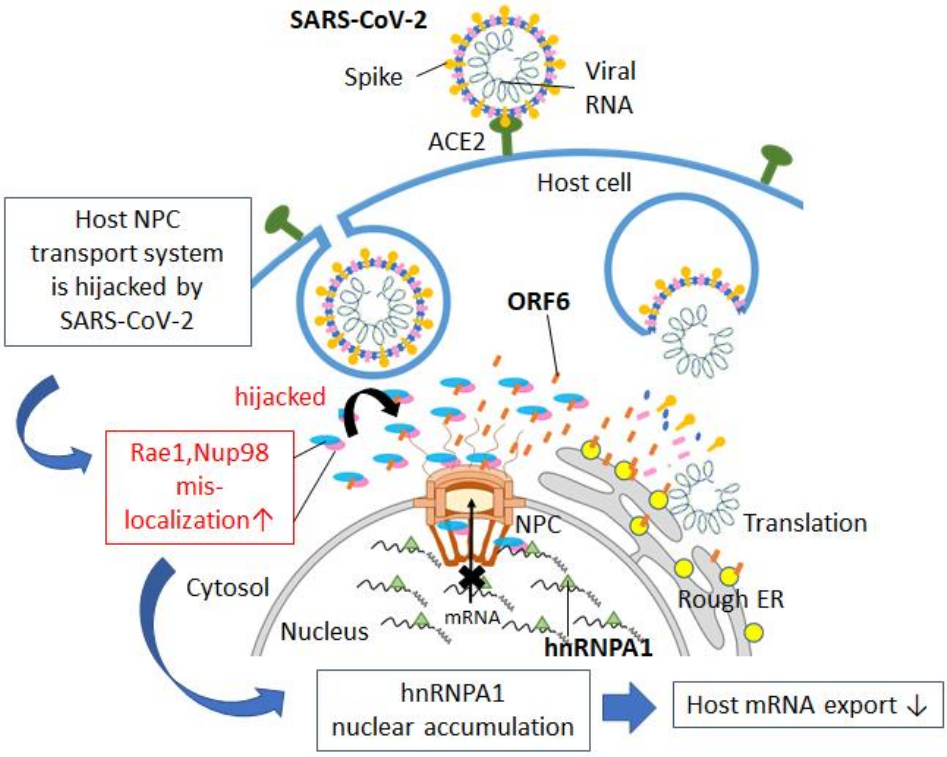

Figure 20. The pathogenesis of SARS-CoV-2 in association with Nucleocytoplasmic trafficking.

II.7. REFERENCES

[1] H. Ben, G. Hua, Z. Peng, L.S. Zheng, Characteristics of SARS-CoV-2 and COVID-19, Nat Rev Microbiol. 19 (2021) 141-154.

[2] Y. Zang, E.C. Holmes, A Genomic Perspective on the Origin and Emergence of SARS-CoV-2, Cell 26 (2020) 223-227.

[3] D. Bojkova, K. Klann, B. Koch, et al., Proteomics of SARS-CoV-2-infected host cells reveals therapy targets, Nature 583 (2020) 469-472.

[4] P. Zhou, X. L. Yang, Z. L. Shi, A pneumonia outbreak associated with a new coronavirus of probable bat origin, Nature 579 (2020) 270–273.

[5] K. Theresa & Ebert, Gregor & Calleja, Dale & Allison, et al., Mechanism and inhibition of the papain-like protease, PLpro, of SARS-CoV-2. The EMBO Journal 10 (2020) 15252.

[6] J.G. Lee, W. Huang, H. Lee, et al., Characterization of SARS-CoV-2 proteins reveals Orf6 pathogenicity, subcellular localization, host interactions and attenuation by Selinexor, Cell & bioscience 58 (2021) 11.

[7] J.R. Babu, K.B. Jeganathan, D.J. Baker, et al., Rae1 is an essential mitotic checkpoint regulator that cooperates with Bub 3 to prevent chromosome missegregation, J. Cell Biol. 160 (2003) 341e353.

[8] R.W.Wong, G. Blobel, E. Coutavas, Rae1 interaction with NuMA is required for bipolar spindle formation, Proc. Natl. Acad. Sci. U.S.A. 103 (2006) 19783e19787.

[9] R.W. Wong, Interaction between Rae1 and cohesin subunit SMC1 is required for proper spindle formation, Cell Cycle 9 (2010) 198e200.

[10] T. R. Lezon, A. Sali, I. Bahar, Global motions of the nuclear pore complex: Insights from elastic network models. PLoS Comput. Biol. 5 (**2009**) e1000496.

[11] K. H. Bui, A. v. Appen, A. L. DiGuilio, et al., Integrated structural analysis of the human nuclear pore complex scaffold. Cell 155 (2013) 1233–1243.

[12] M. Eibauer, M. Pellanda, Y. Turgay et al., Structure and gating of the nuclear pore complex, Nat com. 6 (2015) 7532

[13] B. B. Hülsmann, A. A. Labokha, D. Görlich, The Permeability of Reconstituted Nuclear Pores Provides Direct Evidence for the Selective Phase Model, Cell 4 (2012) 738-751.

[14] R. Y. H. Lim, N. P. Huang, J. Köser, et al., Flexible phenylalanine-glycine nucleoporins as entropic barriers to nucleocytoplasmic transport, Proc. Nat. Acad. Sci. USA. 103 (2006) 9512–9517.

[15] J. A. Hiscox, The interaction of animal cytoplasmic RNA viruses with the nucleus to facilitate replication. Virus Res. 95 (2003) 13-22.

[16] M.K. Weidman, R. Sharma, S. Raychaudhuri, et al., The interaction of cytoplasmic RNA viruses with the nucleus. Science 288 (2000) 1374-1377.

[17] J.Y. Lin, T.C. Chen, K.F. Weng, et al., Viral and host proteins involved in picornavirus life cycle. J. Biomed. Sci. 16 (2009) 103.

[18] E.S. Sajidah, K.S. Lim, R.W. Wong, How SARS-CoV-2 and Other Viruses Build an Invasion Route to Hijack the Host Nucleocytoplasmic Trafficking System, Cells 10 (2021**)** 1424.

[19] E.L.P. Kneller, J.H. Connor, D.S. Lyles, hnRNPs Relocalize to the cytoplasm following infection with vesicular stomatitis virus, J. Virol. 83 (2009) 770e780.

[20] A.C. Francis, G.B. Melikyan, Single HIV-1 imaging reveals progression of infection through CA-dependent steps of docking at the nuclear pore, uncoating, and nuclear transport, Cell Host Microbe 23 (2018) 536e548.

[21] R.W.Wong, J.I. Mamede, T.J. Hope, Impact of nucleoporin-mediated chromatin localization and nuclear architecture on HIV integration site selection, J. Virol. 89 (2015) 9702e9705.

[22] M.R. Fontes, T. Teh, B. Kobe, Structural basis of recognition of monopartite and bipartite nuclear localization sequences by mammalian importin-alpha, J. Mol. Biol. 297 (2000) 1183–1194.

[23] A. Herold, R. Truant, H. Wiegand, B. R. Cullen, Determination of the functional domain organization of the importin alpha nuclear import factor. J. Cell Biol. 143 (1998) 309–318.

[24] E. Conti, M. Uy, L. Leighton, et al., analysis of the recognition of a nuclear localization signal by the nuclear import factor karyopherin alpha, Cell 94 (1998,) 193–204.

[25] D.E. Gordon, G.M. Jang, M. Bouhaddou, et al., A SARS-CoV-2 protein interaction map reveals targets for drug repurposing, Nature 583 (2020) 459e468.

[26] M. Bouhaddou, D. Memon, B. Meyer, et al., The global phosphorylation landscape of SARS-CoV-2 infection, Cell 182 (2020) 685e712.

[27] S. Krull, J. Dörries, B. Boysen, et al., Protein Tpr is required for establishing nuclear pore-associated zones of heterochromatin exclusion, EMBO J. 29 (2010) 1659–1673.

[28] G. M. Hautbergue, M. L. Hung, A. P. Golovanov, et al., Mutually exclusive interactions drive handover of mRNA from export adaptors to TAP, Proc. Nat. Acad. Sci. USA 05 (2008) 5154–5159.

[29] C. Braun, A. Herold, M. Rode, E. Izaurralde, Nuclear export of mRNA by TAP/NXF1 requires two nucleoporin-binding sites but not p15, Mol. Cell. Biol. 22 (2002) 5405–5418.

[30] N.G. Farny, J. A. Hurt, P. A. Silver, Definition of global and transcript-specific mRNA export pathways in metazoans, Genes Dev. 22 (2008) 66–78.

[31] M. B. Blevins, A. M. Smith, E. M. Phillips, M. A. Powers, Complex formation among the RNA export proteins Nup98, Rae1/Gle2, and TAP, J. Biol. Chem. 278 (2003) 20979–20988.

[32] Y. Xie, Y. Ren, Mechanisms of nuclear mRNA export: A structural perspective, Traffic 20 (2019) 829–840.

[33] H. Xia, Z. Cao, X. Xie, et al., Evasion of Type I Interferon by SARS-CoV-2, Cell Rep. 33 (2020) 108234.

[34] S.A. Kopecky-Bromberg, L. Martínez-Sobrido, M. Frieman, et al., Severe acute respiratory syndrome coronavirus open reading frame (Orf) 3b, Orf 6, and nucleocapsid proteins function as interferon antagonists. J. Virol. 81 (2007) 548–557.

[35] A. Addetia, N. A. P. Lieberman, Q. Phung, et al., SARS-CoV-2 Orf6 Disrupts Bidirectional Nucleocytoplasmic Transport through Interactions with Rae1 and Nup98. mBio (2021) 12.

[36] A. Quan, H.S. Seo, G. Blobel, Y. Ren, Vesiculoviral matrix (M) protein occupies nucleic acid binding site at nucleoporin pair (Rae1 _ Nup98), Proc. Natl. Acad. Sci. U.S.A. 111 (2014) 9127e9132.

[37] K.R. Rajani, E.L.P. Kneller, M.O. McKenzie, et al., Complexes of vesicular stomatitis virus matrix protein with host Rae1 and Nup98 involved in inhibition of host transcription, PLoS Pathog. 8 (2012), e1002929, https://doi.org/ 10.1371/journal.ppat.1002929.

[38] Y. Ren, H.-S. Seo, G. Blobel, A. Hoelz, Structural and functional analysis of the interaction between the nucleoporin Nup98 and the mRNA export factor Rae1, Proc. Natl. Acad. Sci. U.S.A. 107 (2010) 10406e10411.

[39] T. Funasaka, H. Nakano, Y. Wu, C. Hashizume, L. Gu, T. Nakamura, W. Wang, P. Zhou, M.A. Moore, H. Sato, R.W. Wong, RNA export factor Rae1 contributes to Nup98-HOXA9-mediated leukemogenesis, Cell Cycle 10 (2011) 1456e1467.

[40] M. Hazawa, K. Sakai, A. Kobayashi, H. Yoshino, Y. Iga, Y. Iwashima, K.S. Lim, D.C. Voon, Y. Jiang, S. Horike, D.C. Lin, R.W. Wong, Disease-specific alteration of karyopherin-a subtype establishes feed-forward oncogenic signaling in head and neck squamous cell carcinoma, Oncogene 39 (2020) 2212e2223.

[41] A. Kobayashi, C. Hashizume, T. Dowaki, R.W. Wong, Therapeutic potential of mitotic interaction the nucleoporin Tpr and aurora kinase A, Cell Cycle 14 (2015) 1447e1458.

[42] F.R.P. Dewi, S. Jiapaer, A. Kobayashi, M. Hazawa, D.K. Ikliptikawati, Hartono, H. Sabit, M. Nakada, R.W. Wong, Nucleoporin TPR (translocated promoter region, nuclear basket protein) upregulation alters MTOR-HSF1 trails and suppresses autophagy induction in ependymoma, Autophagy 24 (2020) 1e12.

[43] M. Hazawa, D.C. Lin, A. Kobayashi, Y.Y. Jiang, L. Xu, F.R.P. Dewi, M.S. Mohamed, Hartono, M. Nakada, M. Meguro-Horike, S.I. Horike, H.P. Koeffler, R.W. Wong, ROCK-dependent phosphorylation of NUP62 regulates p63 nuclear transport and squamous cell carcinoma proliferation, EMBO Rep. 19 (2018) 73e88.

[44] P. Jevti_c, A.C. Schibler, C.C. Wesley, et al., The nucleoporin ELYS regulates nuclear size by controlling NPC number and nuclear import capacity, EMBO Rep. 20 (2019), e47283.

[45] J.R. St-Germain, A. Astori, P. Samavarchi-Tehrani, et al., A SARS-CoV-2 BioIDbased virus-host membrane protein interactome and virus peptide compendium: new proteomics resources for COVID-19 research, bioRxiv 28 (2020) 269175, https://doi.org/10.1101/2020.08.28.269175.

[46] C.K. Yuen, J.Y. Lam, W.M. Wong, et al., SARS-CoV-2 nsp 13, nsp 14, nsp 15 and Orf6 function as potent interferon antagonists, Emerg. Microb. Infect. 9 (2020) 1418e1428.

[47] J.Y. Li, C.H. Liao, Q. Wang, et al., The Orf6, Orf8 and nucleocapsid proteins of SARS-CoV-2 inhibit type I interferon signaling pathway, Virus Res. 286 (2020) 198074.

[48] X. Lei, X. Dong, R. Ma, et al., Activation and evasion of type I interferon responses by SARS-CoV-2, Nat. Commun. 11 (2020) 3810.

[49] A.C. Sims, S.C. Tilton, V.D. Menachery, et al., Release of severe acute respiratory syndrome coronavirus nuclear import block enhances host transcription in human lung cells, J. Virol. 87 (2013) 3885e3902.

[50] F.W. Porter, A.C. Palmenberg, Leader-induced phosphorylation of nucleoporins correlates with nuclear trafficking inhibition by cardioviruses, J. Virol. 83 (2009) 1941e1951.

[51] M.L. Shaw, W.B. Cardenas, D. Zamarin, et al., Nuclear localization of the Nipah virus W protein allows for inhibition of both virus- and toll-like receptor 3- triggered signaling pathways, J. Virol. 79 (2005) 6078e6088.

[52] S.P. Reid, L.W. Leung, A.L. Hartman, et al., Ebola virus VP24 binds karyopherin alpha 1 and blocks STAT1 nuclear accumulation, J. Virol. 80 (2006) 5156e5167.

CHAPTER III. Label-free tomographic imaging of nanodiamonds in living cells (A new promising method to visualize tagged Rae1 in near future)

III.1. ABSTRACT

Given the huge impact of Rae1 in our laboratory's long work history, it is reasonable to consider the new, fast and reliable system dedicating for better labeling and imaging of this protein inside living cells. Nanodiamonds (NDs) have acknowledged growing attention due to their decent biocompatibility and photostability with its application as a molecular label is actually not a new phenomenon. However, despite its extensive utilization, major drawback such as phototoxicity from laser irradiation to detect the fluorescence signal still limits this long-time tracking of nanodiamonds in living cells. Other researcher of our laboratory in collaboration with Kyoto University has succesfully detect Rae1 in a conjugation form with Nanodiamonds (DNDs-HPG-Rae1) using high speed AFM (unpublished data). Prior to achieve future study of new Rae1 visualization method inside living cell facilitated by NDs, here, we performed novel quantitative morphological and biophysical celullar analysis by optical diffraction tomography (ODT) using various sizes and introduction methods of NDs. ODT is an inexpensive and noninvasive microscopy technique, which images cells and subcellular structures as a function of their refractive index (RI); hence, can reduce phototoxicity. In this sudy, the very high RI of NDs in HeLa cells can be clearly discriminated from cellular structures. Aggregation and deaggregation of internalized NDs can be detected via changes in the RI distribution of the entire cell and the prevention of in-cell particle aggregation was observed through polyglycerol coating of NDs. In endocytosis method, optical diffraction tomography shows deaggregation of NDs after a prolonged incubation time. Together, these findings implicate that RI measurements are a favorable tool to track NDs, without a fluorescent label, inside living cells. This could be useful to study real time metabolic activities in living cells using very weak laser irradiation. Also, as our data indicated no significant changes of viability of cells

receiving NDs treatment, we hopefully can continue to bioconjugate Rae1 into NDs and successfully tracked it inside the living cells by ODT in the near future.

Keywords:
Rae1, fluorescence, nanodiamonds, refractive-index tomography, optical diffraction tomography (ODT)

III.2. INTRODUCTION

The study of the role of nucleoporin Rae1 in living cells is strongly correlated to the recombinant protein expression and purification experiments performed multiple times in our laboratory. Additionally, several fusion tags with nups have been developed to support identification and characterization of Rae1 in cancer cell. Protein tags are peptides that are inserted into a translated protein that have a wide range of application; some of them are purification, detection, solubilization, localization, or protease protection [36]. They can also be used to identify potential binding partners of the protein of interest. Our previous studies of Rae1 and other nucleoporins have utilize Hemaglutinin (HA) tag [37], Histidine tag [38], Flag tag [39,40], and GFP tag [41,42]. Despite the superior results yielded from those studies, it is undeniable that such techniques have special preparation that might be labouring. In other hand, these tags system usually followed by laser-based imaging that can raise the possibility of gaining phototoxicity and photobleacing side effect to the living cells. Therefore, this issues encourage us to study the other alternative of faster and less toxic protein labeling-imaging system.

In recent years, nanodiamonds (NDs) have emerged as a highly promising material for various biomedical applications namely fluorescent imaging and drug delivery [1–3]. Due to their extremely stable chemical structure, they are usually regarded to be physically and chemically stable, bioinert, and biocompatible,

making them appealing for use as multifunctional probes [4–6]. NDs are made of carbon, which is compatible with biological systems, unlike other fluorescent nanoparticles that contain heavy metal components like quantum dots. NDs are regarded one of the most biocompatible types of carbon-based nanomaterials, such as fullerenes and carbon nanotubes, since they are made of sp3 carbon, which is relatively unreactive. While the crystalline core of the nanodiamonds is very stable, its surface can be chemically modified, which is a key factor for the particle dispersibility, chemical functionalization and in-cell targeting [7–52 10]. There are two different sources for the fluorescent properties of nanodiamonds [3]. On one hand, there are special crystal defects, so called color centers, where the Nitrogen-Vacancy (NV) center, is the most famous and popular one [4,11]. The NV center, a substitutional nitrogen defect (a nitrogen atom replacing a carbon atom), next to a vacancy (a missing carbon atom), stands out from the crowd of fluorescent bio-labels due to its stable and non-bleaching fluorescence. On the other hand, the fluorescence from nanodiamonds can stem from organic functional groups on the particle surface. These show a stronger fluorescent signal than NV centers, however in combination with photobleaching [12]. In this paper, we present a new method to image nanodiamonds inside cells not based on fluorescence but solely due to their inherent property: the refractive index. Diamond is one of the material with the highest refractive index with $n = 2.425$ at 532 nm [13], which is the secret behind the brilliance of the gem stone. We use the microscopy technique of refractive index tomography (also called optical diffraction tomography or ODT [15]) to generate 64 a three-dimensional (3D) image of nanodiamonds inside the cell. The method can image different cellular structures [14] and can provide quantitative information on biological samples from measured 3-D refractive index (RI) distribution, including protein concentration, cellular dry mass, and volume [16,17]. Recently, the imaging of gold nanoparticles in living cells were demonstrated using ODT [18]. This approach has at least two key advantages over fluorescence detection of nanodiamonds. First, the creation of color centers like NV centers in nanodiamonds are not anymore needed. This step involves ion or electron

irradiation and high temperature annealing, which is time consuming, expensive and needs access to specialized equipment. The chemical modification of fluorescent nanodiamonds before their application requires a large amount of material, which makes this approach even more costly. Second, the detection scheme using ODT is much more efficient, since all scattered light is detected, while the number of fluorescent photons is by many orders of magnitude smaller. As for fluorescence detection of nanodiamonds [11], ODT is not limited to cells, but can be applied to organisms such as *C. elegans*, as long as they are transparent for visible light. As an alternative to fluorescence detection, light scattering had been demonstrated in a few pioneering contributions to identify nanodiamonds inside cells. Smith et al. detected 55 nm nanodiamond particles using differential interference and Hoffman modulation 'space' contrast microscopy, where nanodiamonds can appear up to 300 times brighter than a cell organelle of the same size [19]. Chao et al. presented Raman mapping as a non-invasive imaging method, where spots with the characteristic Raman resonance for sp3 carbon at 1332 cm-1 selectively filtered the presence of 100 nm nanodiamonds [20]. And recently, Khanal et al. used holotomography to image the cell uptake of nanodiamonds [21]. However, none of this work had extracted detailed RI distributions to analyze protein a ggregation or formation of protein corona of NDs inside cells, as we show in this paper. The RI values of NDs were substantially greater than other intracellular components in cells, according to the observed tomograms. NDs were effectively separated from cytoplasm with high spatial resolution using this fact, which was validated by confocal fluorescence imaging of nanodiamonds with NV centers. We statistically evaluated the volume distribution of aggregated NDs and the time development of NDs volume ratios inside the HeLa cell line using the present approach, which gave quantitative information regarding NDs accumulation inside cells. We compared two different internalization methods, endocytosis and electroporation, for the uptake of nanodiamonds. Nanodiamonds of three different sizes, 5 nm, 35 nm and 100 nm were applied and the effect of a polymer coating with hyper-branched polyglycerol (HPG) [22], making the nanodiamonds resistant to aggregation, was

studied. 5 nm nanodiamonds are so-called detonation nanodiamonds (DNDs), which are the smallest commercially available NDs and were recently enriched in NV centers [23,24].

III.3. MATERIALS AND METHODS

III.3.1. Nanodiamonds materials

Detonation Nanodiamonds (DNDs) of ca. 5 nm were generously donated by Professor Eiji Ōsawa, NanoCarbon Research Institute, Ltd (Ueda, Japan). 100 nm sized nanodiamonds Micron+MDA were purchased from Element Six. 96% glycidol was purchased from Sigma Aldrich. Fluorescent nm nanodiamonds were purchased from FND Biotech, Taiwan ("brFND-35").

III.3.2. Creation of NV centers in nanodiamonds

The Creation of NV centers in nanodiamonds was conducted in Department of Molecular Engineering, Graduate School of Engineering, Kyoto University. Nanodiamond powder was irradiated with a 2 MeV electron beam at a fluence of 1 × 1018 e−/cm2 (10 h), followed by thermal annealing in vacuum at 800 °C for 2 h and oxidation in air at 550 °C for 2 h. Synthesis of Hyper-branched polyglycerol (HPG)-coated NDs HPG coating of nanodiamonds was prepared as described in Ref. [22].

III.3.3. Optical Diffraction Tomography (ODT)

Three-dimensional reflective index tomographic analysis was described in Refs. [32,33]. The 3D RI distribution of NDs was reconstructed by commercialized ODT setups (H1-H, Tomocube, Inc., South Korea) based on an off-axis Mach-Zehnder interferometer assembled with a digital micromirror device (DMD) unit (Texas InstrumentsTM). A diode-pumped solid state laser (λ =

532nm; 0,05mW; laser class1) (specification, company beam was 266 divided into two arms by a beam splitter. One arm was used as a reference beam and the other one illuminated a sample with various illumination angles which is controlled Multiple 2D optical field images were measured at various illumination angles.

III.3.4. Stimulation-free (Endocytosis-NDs internalization)

Human cervical cancer cells (HeLa cells) in Dulbecco's modified Eagle's medium (DMEM) was cultured at 1.5x105 cells per tomodish (©Tomocube, Inc.) and incubated for 24 h at 37°C in a humidified atmosphere containing 5% CO2. On the day of treatment, each NDs (5nm-ND, 35nm-ND, 100nm-ND, 30nm HPG-ND, and 100nm HPG-ND) was added to the culturing medium at a final concentration of 10 μg/mL and observed after 3 and 6 h incubation time.

III.3.5. Electroporation

The Neon® Transfection System (Invitrogen, MPK500) was used for electroporation. One day prior to electroporation, cells were transfered into dish with fresh Dulbecco's Modified Eagle's Medium (DMEM) (Wako,043-30085) supplemented with 10% (v:v) fetal bovine serum (FBS) (Life Technologies, 10082147) such that the cells are 70-90% confluent on the day of the experiment. An aliquot of DMEM+FBS, Ca2+ and Mg2+ free-phosphate-buffered saline (-/-PBS) (137 mM NaCl (Nacalai Tesque, 31320-34), 2.7 mM KCl (Sigma, P9541), 10 mM Na2HPO4 (WAKO, 198-05955F), 1.8 mM KH2PO4(Nacalai Tesque, 28736-750), and Trypsin/EDTA (Nacalai Tesque, 32777-15) were pre-warmed to 37ºC. The medium from cells was aspirated and the cells were rinsed using -/-PBS. Cells were trypsinized using Trypsin/EDTA. After neutralization, the cells were harvested 289 in ~0.75 mL medium with serum. Cells on an aliquoted of trypsinized cell suspension was then counted to determine the density. The cells were transfered to a 1.5 mL microcentrifuge tube and centrifuged at 400 × g for 5

minutes at room temperature. Cells were washed with -/-PBS by centrifugation at 400 × g for 5 minutes at room temperature. PBS was aspirated and the cell pellet was resuspended in Resuspension Buffer R (Neon® Kits, MPK1096) containing NDs (5nm-ND, 5nm HPG-COOH-NHS-ND, 35nm-ND, 100nm-ND, and 100nm HPG-ND) at a final concentration of 10 μg/mL and final cell density of 1.0 × 107 cells/mL. Cells were gently pipetted to obtain a single cell suspension. Cell suspension was then drawn by Neon® pipette with inserted 10 μL Neon® Tip. The electrical pulses were delivered at 1700 V, 10 mS, 1x pulse. Immediately after electroporation, cells were placed in tomodish (©Tomocube, Inc.) and 6-well plates with DMEM (Wako,043-30085) + FBS (Life Technologies, 10082147) without antibiotics and incubated at 37˚C for 16 h.

III.3.6. Immunostaining and super-resolution imaging

The 6-well plates equipped by glass coverslips and collagen coating (Sigma, C3867) were prepared to culture HeLa cells. Cells on coverslips were then washed with PBS and fixed for 30 minutes with 4% paraformaldehyde in PBS. The washing step with PBS was repeated, and cells were permeabilized with 0.3% Triton X-100 in PBS for 3 minutes. Cells were washed again before blocked in PBS with 4% BSA at room temperature for 30 minutes. Incubation overnight of the coverslips were performed in 4% BSA/PBS supplemented with primary antibodies at dilution of 1:100. Next, cells were rinsed and the incubation with secondary antibodies were performed in 4% BSA/PBS at dilution of 1:100 dilution at room temperature for 2 hours. After PBS washing, The surface of coverslips with cells was then attached on slides and mounted by ProLong Diamond Antifade reagent with DAPI (DAPI; Invitrogen, 311 P36941). The observation was performed using confocal laser-scanning microscope with 60X PlanApo/1.45NA DIC objective (Leica, TCS SP8).

III.3.7. Cell proliferation assay

Cells with a density of $3x10^3$ cells per well of HeLa and MCF7 cells treated with various NDs by direct dispersion and electroporation were plated and incubated into 96 wells plates for the specified period. The MTT (3-(4, 5-dimethylthiazol-2-yl)-2, 5-diphenyltetrazolium bromide) technique was used to determine cell viability. Specifically, every wells were added by 10 µL of MTT, followed by 3 hours incubation and 100 µL stop solution (2 % acetic acid, 16 % SDS, 42 % DMF) to terminate the reaction. The 570 nm absorbancy was used to measure the samples after they had been properly mixed.

III.4. RESULTS

III.4.1. NDs showing no significant effect on cell's viability

First, to determine whether or not NDs affects cell viability, we performed MTT assay on HeLa and MCF7 cell lines incubated by various types of NDs and introduction methods. The results showed that there was no significant change of cell growth observed in all ND-treated cell conditions including NDs sizes (5,35, and 100nm ND), surface modification (30 and 100 nm HPG), and introduction methods (electroporation vs endocytosis) compare to control cell, suggesting that NDs might has no (or very limited) cytotoxic effect inside the cells (**Figure 21**).

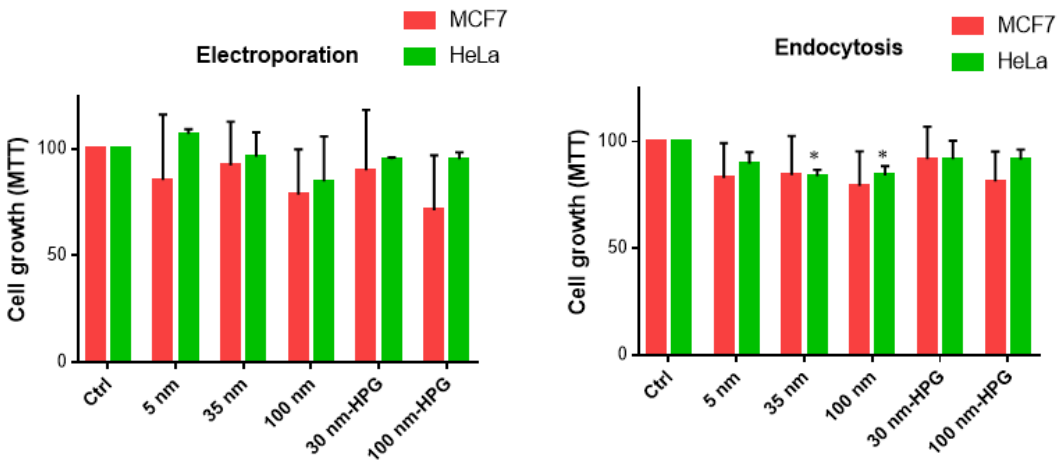

Figure 21. The effects of NDs on cell viability (n = 3, mean ± SD). One sample *t* test was performed using GraphPad Quick Calcs. *$p < 0.05$.

III.4.2. NDs in HeLa cell can be visualized using Confocal Microscopy

In order to determine localization of ND inside cells, we performed confocal microscopic imaging of NDs with different sizes containing NV centers introduced into HeLa cells by electroporation. To determine subcellular localization, nucleoporins (NUPs) with Phenylalanine-Glycine repeat (FG), components of the nuclear pore complex (NPC), was visualize by immunofluorescence staining (**Figure 22.A**). NPC is constructed by 30 different proteins called NUP. One-third of NUP have Phenylalanine-Glycine repeat (FG), those are called FG-NUP. M414 antibody recognizes those several FG-NUPs. Therefore, the green color indicates NPC or FG-NUPs, the red colorstemming from NV centers, indicates NDs. Consistent with previous study [25], those NDs were observed in cytoplasm and did not enter the nuclei. These NDs were not coated with a polymer (HPG) and are therefore prone to aggregate inside cells. Further, HeLa cells without ND never showed fluorescent signaling (570 – 700 nm) (**Figure 22.B**), proving successful detection of ND fluorescent signaling.

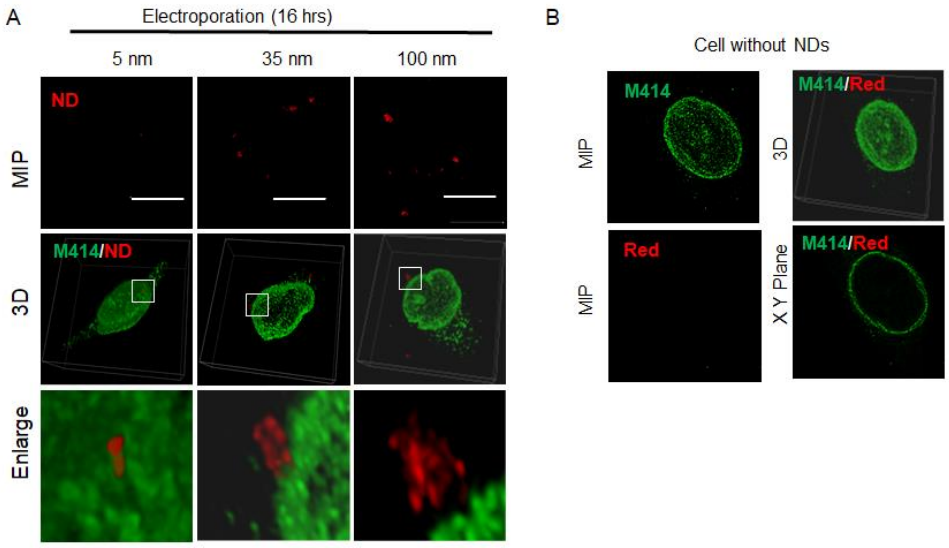

Figure 22. Visualization of NDs in HeLa cell using Confocal Microscopy. **A**. Cell treated with 5 nm, 35 nm, and 100 nm of NDs, immunostained with M414 antibody. **B**. Fluorescence images of the native cell. Scale bar is 5 µm. MIP stands for maximum intensity projection.

III.4.3. Tomographic imaging of NDs in HeLa cell introduced by electroporation showing size-dependency pattern.

Next, first series of refractive-index imaging experiments were performed using electroporation of NDs with three different sizes in HeLa cells. **The Figure. 23.A** shows the representative RI tomograms. The purple and green colors were applied for mapping particular RI values of tomograms (see color bar in **Figure. 23.A**). **Figure. 23.B** shows RI histograms, taken over n = 10 ND treated HeLa cells. The RI values decreased with the size of nanodiamonds. Thereby, 100 nm-NDs showed clearly the largest values, while 35-nm and 5-nm nanodiamonds showed a rather similar RI distribution profile. The empty cell ("control") showed the lowest RI distribution of all four data sets. **Figure. 23.C** shows the statistical analysis for RI > 1.39, a range, which is above the RI of cellular structure [14].

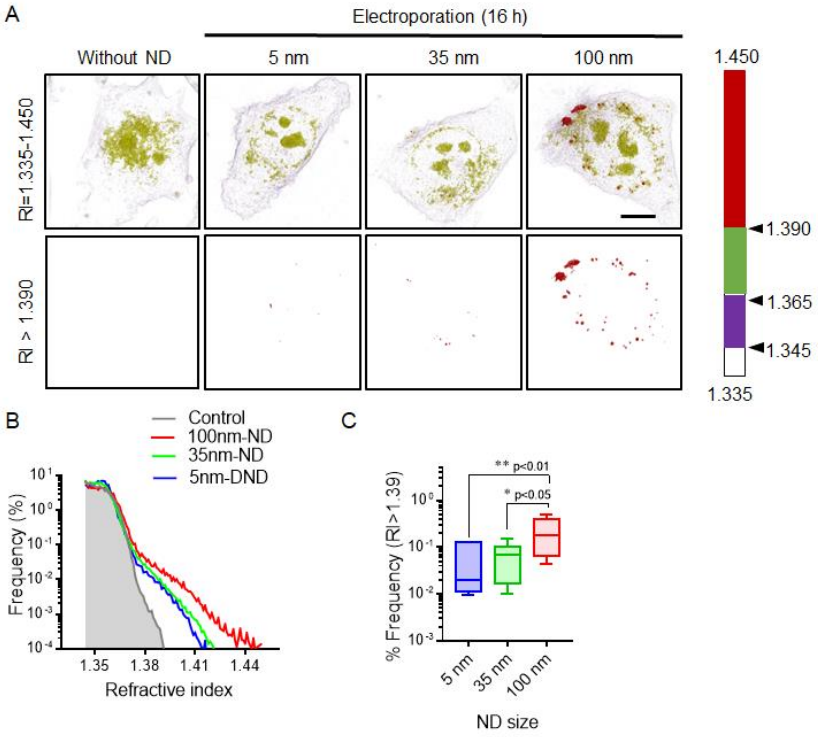

Figure 23. Size-dependency tomographic imaging of NDs in HeLa cell introduced by electroporation. **A**. 3-D RI tomogram of native cell and cell treated with NDs (5nm, 35 nm, and 100 nm). Scale bar is 5 µm. **B** Average RI histograms of native and NDs treated cells (n = 10). **C** Box-whisker plots to compare the frequency distribution (in %) of RI > 1,39 for 5 nm, 35 nm, and 100 nm NDs. Box plot element: medians with interquartile range and whiskers (min to max). Asterisks represent significant difference (P value) according to unpaired two-tailed *t*-test.

III.4.4. Tomographic imaging of NDs in HeLa cell introduced by endocytosis showing size-dependency pattern.

In a second series HeLa cells after endocytosis of NDs were imaged (**Figure 24.A**). **Figure 24. B** and **C** plotting are the same evaluation as in **Figure 23. B** and **C**. Again, the RI distribution decreases with the size of nanodiamonds. However, in contrast to the electroporation data, the RI values of the 5 nm and 35 nm NDs are much closer to the 100 nm NDs.

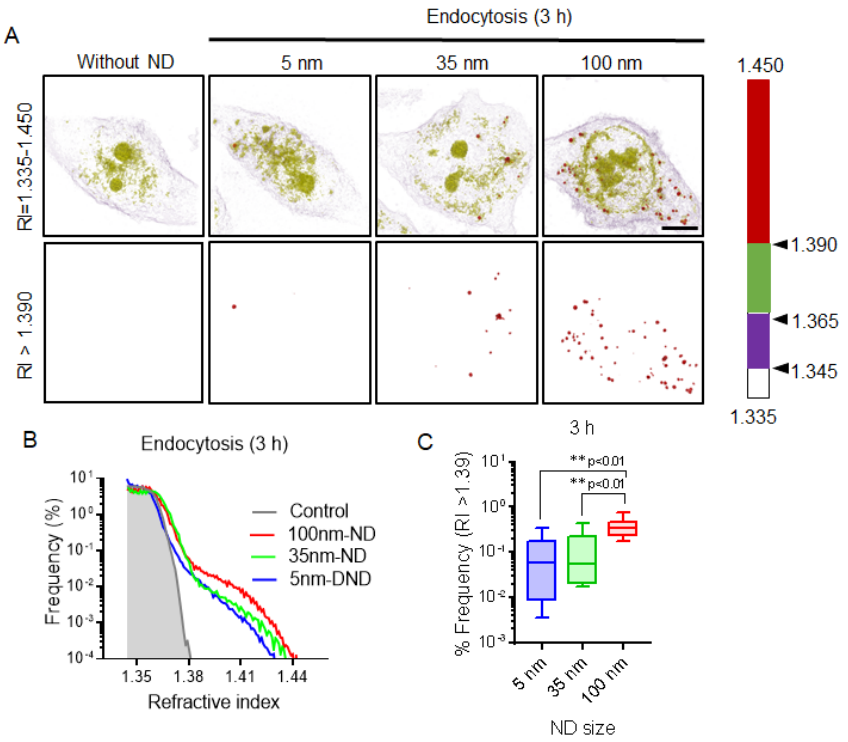

Figure 24. Size-dependency tomographic imaging of NDs in HeLa cell introduced by endocytosis. **A**. 3-D RI tomogram of native cell and cell treated with NDs (5nm, 35 nm, and 100 nm). Scale bar is 5 µm. **B**. Average RI histograms of native and NDs treated cells (n = 10). **C**. Box-whisker plots to compare the frequency distribution (in %) of RI > 1,39 for 5 nm, 35 nm, and 100 nm NDs. Box plot element: medians with interquartile range and whiskers (min to max). Asterisks represent significant difference (P value) according to unpaired two-tailed *t*-test.

III.4.5. Tomographic imaging of NDs in HeLa cell introduced by endocytosis showing time-dependency pattern.

In a third series, we compared different incubation times, 3 h and 6 h, after NDs introduction through endocytosis in order to see the effects of interaction between intracellular components and NDs on RI of NDs. As shown in **Figure 25. A**, NDs aggregation for 6 h incubation became smaller than those in 3 h incubated cells. The quantitative measurements of RI intensity were uniformly proceeded. The RI distribution for the longer incubation time was significantly lower and the size of aggregates became smaller (see **Figure 25. B** and **C**).

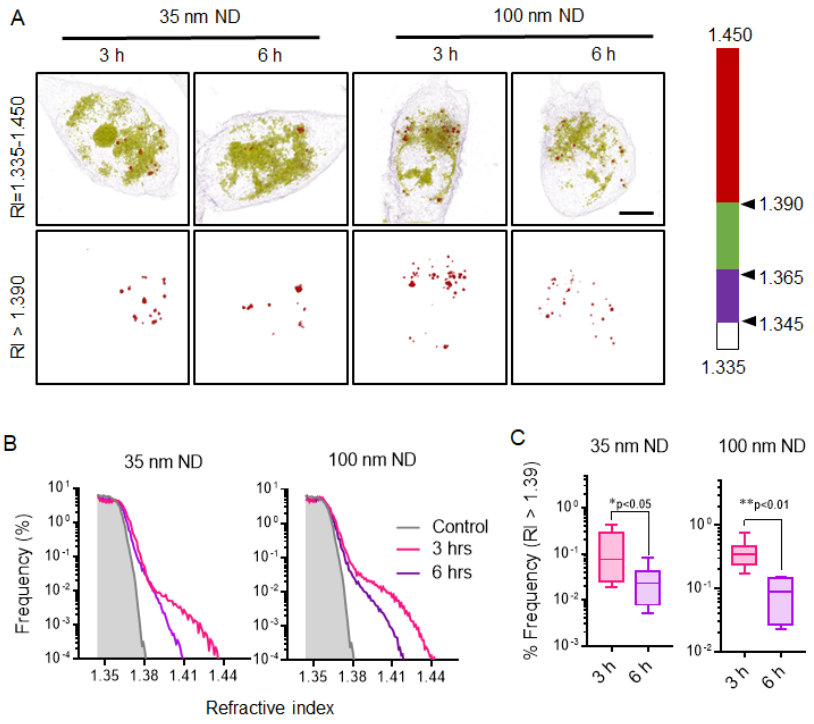

Figure 25. Time-dependency tomographic imaging of NDs in HeLa cell introduced by endocytosis. **A** 3-D RI tomogram of cell treated with 35nm and 100 nm of NDs at different incubation times (3 hours vs 6 hours). Scale bar is 5 µm. **B**. Average RI histograms of NDs treated cells (n = 10). **C**. Box-whisker plots to compare frequency distribution (in %) of RI > 1,39 for 35 nm, and 100 nm NDs at 3 and 6 hours. Box plot element: medians with interquartile range and whiskers (min to max). Asterisks represent significant difference (P value) according to unpaired two-tailed *t*-test.

III.4.6. Tomographic imaging of NDs in HeLa cell introduced by endocytosis and electroporation showing Coating-dependency pattern.

In a forth series, to determine the effects of HPG coating on intracellular dynamics of NDs, we compared the 100 nm ND either with or without HPG coating, which were introduced in different methods (electroporation and endocytosis). As expected, the polymer-coated NDs, protected from particle aggregation, showed a significantly lower RI distribution (**Figure 26.A-C**). Those trends are observed for both NDs introduction methods, however more pronounced for electroporation (**Figure 26.C**).

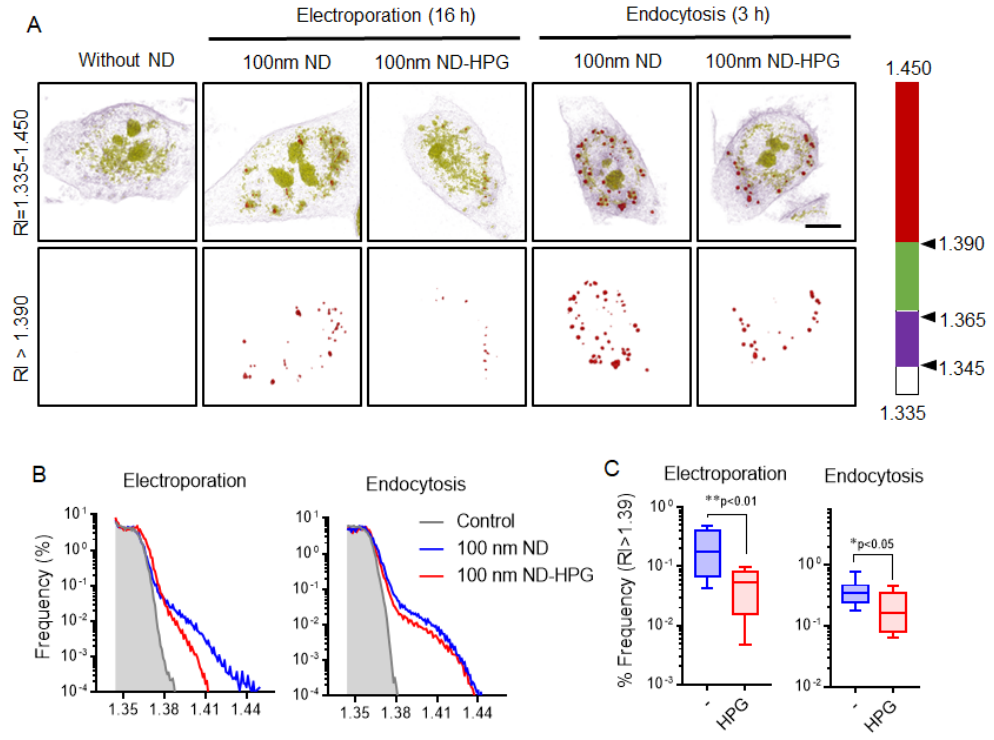

Figure 26. Coating-dependency tomographic imaging of NDs in HeLa cell introduced by endocytosis and electroporation. **A**. 3-D RI tomogram of native cell and cell treated with NDs (100 nm NDs and 100 nm HPG-NDs). Scale bar is 5 µm. **B**. Average RI histograms of native and NDs treated cells (n = 10). **C**. Box-whisker plots to compare the frequency distribution (in %) of RI > 1,39 for 100 nm NDs and 100 nm HPG-NDs at different introduction pathway (endocytosis vs electroporation). Box plot element: medians with interquartile range and whiskers (min to max). Asterisks represent significant difference (P value) according to unpaired two-tailed *t*-test.

III.5. DISCUSSION

All our experiments showed that nanodiamonds, thanks to their high RI values, can be successfully imaged inside cells and can be clearly discriminated from cellular structures using ODT. Beside their detection in RI tomograms, ODT provides an additional dimension through the analysis of the RI distribution over the whole cell. The effective average RI histogram of one voxel (3D confocal volume) can be calculated using the effective medium approximation [18,26] of two substances, in our case water and diamond (see SI). The higher the effective

average RI value, the higher the ND concentration in the detected voxel. Therefore, an increased RI distribution is an indication for nanodiamond aggregation. Besides this, the RI value could be influenced by the surface properties of nanodiamonds: non-diamond carbon, polymer-coating or protein corona [27] formation could decrease the RI value. Since an independent measurement of RI value of nanodiamonds is very challenging [28], these two factors cannot be clearly separated from each other.

We can now analyze the obtained results of RI values in this context. For the first series of ND cell uptake by electroporation (Fig. 2), we observed a decreasing RI value with decreasing ND size. This is expected, since a single 100 nm nanodiamond in a voxel will take a larger volumetric fraction than 35 nm or 5 nm NDs. On top of this, small particles have a larger surface-to-volume ratio, where effects like coverage by a protein corona will more strongly reduce the RI. In the second series, ND cell uptake by endocytosis was studied (Figs. 3 and 4). A remarkable reduction of RI values for 100 nm NDs were observed when the incubation time was doubled from 3 h to 6 h. This speaks for a disaggregation of ND particles with longer incubation time, which could be caused by a protein corona formation and is in agreement with Ref. [27], where a prior coating of the NDs with proteins from cellular medium (FBS) is an effective option to prevent inter-particle aggregation and achieve size reduction. In the third series of experiments using electroporation, we see a similar reduction of RI values for 100 NDs, when coated with a HPG polymer layer, which protects from aggregation (Fig. 5). This result is visible from the RI tomogram in the case of 100 nm NDs showing smaller spot sizes (Fig. 5A). This demonstrates the effectiveness of HPG coating to prevent NDs of different sizes from aggregation after cellular uptake.

A strong advantage of ODT over fluorescence detection is the very weak laser power of only 0.05 mW (only about 5 % of a conventional laser pointer). The accelerated cell death through laser irradiation is one of the major problems for long-time observations of living cells [29]. At the same time, the high sensitivity opens the way for a high temporal resolution enabling the study of dynamic processes, since a 3D image is recorded in less than a second. Especially

for our case of NDs, the fluorescence of NV centers is weak compared to other fluorophores [30] and makes the detection of small NDs containing less NV centers inside cells challenging needing high laser power and expensive and highly-sensitive photon detectors. Last but not least, ODT simplifies experiments tremendously, since the creation of NV centers is not anymore needed for optical detection.

What are the limitations of the methods? As for every microscopy technique, the spatial resolution of ODT is diffraction limited (although this is notably improved in this technique by up to a factor of two [15]). The refractive index for one voxel is the average over all substances present in this volume. Especially, for very small particles such as our 5 nm nanodiamonds, the detection of single isolated particles become difficult, however it should be possible for 100 nm nanodiamonds (see SI). In the case of fluorescence, the spatial resolution is also limited but the photon counts of a fluorophore are not averaged, making single molecule detection a standard experiment. Using fluoresce imaging, even with a highly sensitive microscope, the currently detectable ND size is limited to ca. 20 nm, since the fluorescence from NV centers in smaller NDs is instable and shows blinking and bleaching [31]. Therefore, 5 nm ND spots visible in fluorescence images are limited to aggregated spots. With this in mind, we cannot exclude that 5 nm were present inside the cell nucleus, but cannot prove it with our current detection schemes.

III.6. CONCLUSION

Nanodiamonds (NDs) with their high RI are ideal particles to be visualized by ODT. Internalized NDs can be detected inside a living cell within less than a second and can be clearly discriminated from cellular structure. The very weak usage of laser irradiation in ODT was able to ensure the prolonged cells' life span while performing experiment (**Figure 27)**. This fundamental new method of NDs imaging can give many benefits in the future study; specifically NPC in our field, as the bioconjugation of Rae1 in the NDs (DNDs-HPG-Rae1) has also been successfully detected using high speed AFM.

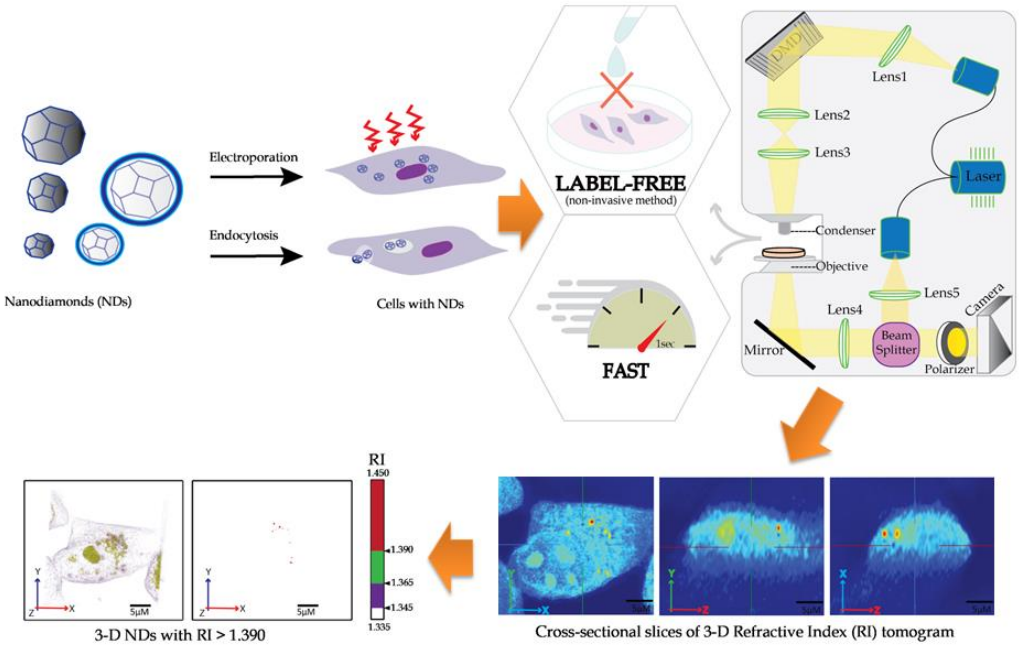

Figure 27. The principle and advantage of ODT to visualize NDs in a living cell

III.7. REFERENCES

[1] V. N. Mochalin, O. Shenderova, D. Ho, Y. Gogotsi, The properties and applications of nanodiamonds, Nat Nanotechnol. 7 (2011) 11–23.

[2] V. Vaijayanthimala, D. K. Lee, S. V. Kim, et al., Nanodiamond-mediated drug delivery and imaging: challenges and opportunities. Expert Opin Drug Deliv 12(2015)735–49.

[3] K. Turcheniuk, V.N. Mochalin, Biomedical applications of nanodiamond (Review). Nanotechnology 28 (2017) 252001.

[4] S. J. Yu, M. W. Kang, H. C. Chang, et al., Bright Fluorescent Nanodiamonds: No Photobleaching and Low Cytotoxicity, J Am Chem Soc. 127(2005)17604–5.

[5] C. C. Fu, H. Y. Lee, K. Chen, et al., Characterization and application of single fluorescent nanodiamonds as cellular biomarkers, Proc Natl Acad Sci U S A. 104(2007)727–32.

[6] A. M. Schrand, H. Huang, C. Carlson, et al., Are Diamond Nanoparticles Cytotoxic ? J Phys Chem B. 111(2007)1–7.

[7] Krueger, New carbon materials: Biological applications of functionalized nanodiamond materials, Chem - A Eur J. 14(2008)1382–90.

[8] Krueger, D. Lang, Functionality is key: Recent progress in the surface modification of nanodiamond, Adv Funct Mater. 22(2012)890–906.

[9] J. Neburkova, J. Vavra, P. Cigler, Coating nanodiamonds with biocompatible shells for applications in biology and medicine, Curr Opin Solid State Mater Sci. 21(2017) 43–53.

[10] D. Terada, T. Genjo, T. F. Segawa, R. Igarashi, M. Shirakawa, Nanodiamonds for bioapplications–specific targeting strategies. Biochim Biophys Acta - Gen Subj. 1864(2020)129354.

[11] R. Igarashi, Y. Yoshinari, H. Yokota, et al., Real-time background-free selective imaging of fluorescent nanodiamonds in vivo, Nano Lett. 12(2012)5726–32.

[12] P. Reineck, D.W.M. Lau, E. R. Wilson, et al., Effect of Surface Chemistry on the Fluorescence of Detonation Nanodiamonds, ACS Nano. 11(2017)10924–34.

[13] H. R. Phillip, E. A. Taft. Kramers-Kronig Analysis of Reflectance Data for Diamond. Phys Rev. (1964) 136.

[14] W. Choi, C. Fang-Yen, K. Badizadegan, et al., Tomographic phase microscopy. Nat Methods. 4(2007)717–9.

[15] Y. Sung, W. Choi, C. Fang-Yen, et al., Optical diffraction tomography for high resolution live cell imaging. Opt InfoBase Conf Pap. 17(2009)1977–9.

[16] K. Kim, S. Lee, J. Yoon, J. Heo, et al., Three-dimensional label-free imaging and quantification of lipid droplets in live hepatocytes. Sci Rep. 6(2016)1–8.

[17] J. Yoon, K. Kim, H. Park, et al., Label-free characterization of white blood cells by measuring 3D refractive index maps, Biomed Opt Express. 6(2015)3865.

[18] D. Kim, N. Oh, K. Kim, S. Y. Lee, et al., Label-free high-resolution 3-D imaging of gold nanoparticles inside live cells using optical diffraction tomography, Methods. 136(2018)160–7.

[19] R. Smith, M. Niebert, T. Plakhotnik, A. V. Zvyagin, Transfection and imaging of diamond nanocrystals as scattering optical labels, J Lumin. 127 (2007) 260–3.

[20] J. I. Chao, E. Perevedentseva, P. H. Chung, et al., Nanometer-sized diamond particle as a probe for biolabeling, Biophys J. Elsevier. 93 (2007) 2199–208.

[21] A. Khanal, Q. Lei, G. Pinget, et al., The protein corona determines the cytotoxicity of nanodiamonds: implications of corona formation and its remodelling on nanodiamond applications in biomedical imaging and drug delivery, Nanoscale Adv. 2 (2020) 4798–812.

[22] L. Zhao, T. Takimoto, M. Ito, et al., Chromatographic separation of highly soluble diamond nanoparticles prepared by polyglycerol grafting, Angew Chemie - Int Ed. 50(2011)1388–92.

[23] D. Terada, T. F. Segawa, A. I. Shames, et al., Monodisperse Five-Nanometer-Sized Detonation Nanodiamonds Enriched in Nitrogen-Vacancy Centers, ACS Nano. 13(2019) 6461–8.

[24] T. F. Segawa, A. I. Shames, How to Identify, Attribute, and Quantify Triplet Defects in Ensembles of Small Nanoparticles, J Phys Chem Lett. 11(2020) 7438–42.

[25] H. M. Leung, M. S. Chan, L. S. Liu, et al., Dual-Function, Cationic, Peptide-Coated Nanodiamond Systems: Facilitating Nuclear-Targeting Delivery for Enhanced Gene Therapy Applications. ACS Sustain Chem Eng. 6 (2018) 9671–81.

[26] D. Stroud, The effective medium approximations: Some recent developments. Superlattices Microstruct. 23(1998)567–73.

[27] S. R. Hemelaar, A. Nagl, F. Bigot, et al., The interaction of fluorescent nanodiamond probes with cellular media, Microchim Acta. 184(2017)1001–9.

[28] S. Person, B. Deutsch, A. Mitra, L. Novotny. Material-specific detection and classification of single nanoparticles, Nano Lett. 11(2011) 257–61.

[29] J. Icha, M. Weber, J. C. Waters, C. Norden, Phototoxicity in live fluorescence microscopy, and how to avoid it, BioEssays 39(2017)1–15.

[30] P. Reineck, B. C. Gibson, Near-Infrared Fluorescent Nanomaterials for Bioimaging and Sensing, Adv Opt Mater. (2017) 5.

[31] C. Bradac, T. Gaebel, N. Naidoo, et al., Observation and control of blinking nitrogen-vacancy centres in discrete nanodiamonds. Nat Nanotechnol. 5 (2010) 345–9.

[32] M. Hazawa, K. Sakai, A. Kobayashi, et al., Disease-specific alteration of karyopherin- α subtype establishes feed-forward oncogenic signaling in head and neck squamous cell carcinoma, Oncogene 39 (2020) 2212–23.

[33] M. Shaaban, M. Hazawa, A. Kobayashi, et al., Biomaterials Spatiotemporally tracking of nano-bio fi laments inside the nuclear pore complex core, Biomaterials 256 (2020)120198.

[34] F.R.P. Dewi, S. Jiapaer, A. Kobayashi, et al., Nucleoporin TPR (translocated promoter region, nuclear basket protein) upregulation alters MTOR-HSF1 trails and suppresses autophagy induction in ependymoma. Autophagy 17(2020)1001–12.

[35] S.Y. Ong, M. Chipaux, A. Nagl, R. Schirhagl, Shape and crystallographic orientation of nanodiamonds for quantum sensing. Phys Chem Chem Phys. 19(2017)10748–52.

[36] C.L. Young, T. Zachary, Britton, A.S. Robinson. Recombinant protein expression and purification: A comprehensive review of affinity tags and microbial applications. Biotechnol. J. 7 (2012) 620–634.

[37] R.W.Wong, G. Blobel, E. Coutavas, Rae1 interaction with NuMA is required for bipolar spindle formation, Proc. Natl. Acad. Sci. U.S.A. 103 (2006) 19783e19787.

[38] Y. Ren, H. S. Seo, G. Blobel, A. Hoelz, Structural and functional analysis of the interaction between the nucleoporin Nup98 and the mRNA export factor Rae1, Proc. Natl. Acad. Sci. U.S.A. 107(2010) 10406-11.

[39] R.W. Wong, G. Blobel, Cohesin subunit SMC1 associates with mitotic microtubules at the spindle pole, Proc. Natl. Acad. Sci. U. S. A 105 (2008) 15441e15445.

[40] R. W. Wong, Interaction between Rae1 and cohesin subunit SMC1 is required for proper spindle formation, Cell Cycle 9 (2010) 198e200.

[41] T. Funasaka, H. Nakano, Y. Wu, C. Hashizume, L. Gu, T. Nakamura, W. Wang, P. Zhou, M.A. Moore, H. Sato, R.W. Wong, RNA export factor RAE1 contributes to NUP98-HOXA9-mediated leukemogenesis, Cell Cycle 10 (2011) 1456e1467.

[42] K. Kato, D.K. Ikliptikawati, A. Kobayashi., et al, Overexpression of SARS-CoV-2 protein Orf6 dislocates Rae1 and Nup98 from the nuclear pore complex, Biochem biophys Res Com. 536 (2021) 59-66.